RESEARCH ARTICLE

Key Points:
- The M_w 8.0 2006 and M_w 7.6 2009 Tonga compressional earthquakes were intraslab ruptures
- Both events activated aftershocks on the megathrust and near the trench
- Regional interplate coupling in southern Tonga appears to be low, with few large thrust earthquakes

The 3 May 2006 (M_w 8.0) and 19 March 2009 (M_w 7.6) Tonga earthquakes: Intraslab compressional faulting below the megathrust

Qingjun Meng[1], David S. Heeszel[2], Lingling Ye[1], Thorne Lay[1], Douglas A. Wiens[3], Minghai Jia[4], and Phil R. Cummins[5]

[1]Department of Earth and Planetary Sciences, University of California, Santa Cruz, California, USA, [2]Office of New Reactors, U.S. Nuclear Regulatory Commission, Washington, Dist. of Columbia, USA, [3]Department of Earth and Planetary Sciences, Washington University, Saint Louis, Missouri, USA, [4]Community Safety and Earth Monitoring Division, Geoscience Australia, Symonston, ACT, Australia, [5]Research School of Earth Sciences, Australian National University, Acton, ACT, Australia

Abstract The Tonga subduction zone is among the most seismically active regions and has the highest plate convergence rate in the world. However, recorded thrust events confidently located on the plate boundary have not exceeded M_w 8.0, and the historic record suggests low seismic coupling along the arc. We analyze two major thrust fault earthquakes that occurred in central Tonga in 2006 and 2009. The 3 May 2006 M_w 8.0 event has a focal mechanism consistent with interplate thrusting, was located west of the trench, and caused a moderate regional tsunami. However, long-period seismic wave inversions and finite-fault modeling by joint inversion of teleseismic body waves and local GPS static offsets indicate a slip distribution centered ~65 km deep, about 30 km deeper than the plate boundary revealed by locations of aftershocks, demonstrating that this was an intraslab event. The aftershock locations were obtained using data from seven temporary seismic stations deployed shortly after the main shock, and most lie on the plate boundary, not on either nodal plane of the deeper main shock. The fault plane is ambiguous, and investigation of compound rupture involving coseismic slip along the megathrust does not provide a better fit, although activation of megathrust faulting is responsible for the aftershocks. The 19 March 2009 M_w 7.6 compressional faulting event occurred below the trench; finite-fault and W-phase inversions indicate an intraslab, ~50 km deep centroid, with ambiguous fault plane. This event also triggered small megathrust faulting. There continues to be a paucity of large megathrust earthquakes in Tonga.

1. Introduction

The Tonga subduction zone (Figure 1) is the most active region of global mantle seismicity but historically has not produced many great shallow plate boundary underthrusting earthquakes like those found in most other circum-Pacific subduction zones [e.g., *Pacheco et al.*, 1993]. There is a corresponding lack of major historical tsunami [*Okal et al.*, 2004, 2011]. This has prompted numerous researchers to infer that the Tonga subduction zone is seismically weakly coupled, with low potential for producing huge ($M_w > 8.5$) earthquakes with massive tsunami [e.g., *Ruff and Kanamori*, 1983; *Christensen and Ruff*, 1988; *Pacheco et al.*, 1993; *McCaffery*, 1997].

Northern Tonga has an exceptionally high trench convergence rate (up to 24 cm/yr) due to rapid Lau Basin back-arc spreading rate (up to 15 cm/yr) [e.g., *Bevis et al.*, 1995] and, like southern Tonga, may have very low coupling [e.g., *Scholz and Campos*, 1995, 2012]. However, it is clear that the seismological record is very short and may be misleading with respect to great earthquake potential. GPS measurements along the island arc are located far from the trench and are, as yet, unable to resolve slip-deficit accumulation on the megathrust [e.g., *Wallace et al.*, 2005]. The high trench convergence rate and great length (~1100 km) of the Tonga subduction zone provide a tectonic context that could potentially support a low-probability maximum magnitude event of M_w~8.57 to ~9.14 [e.g., *McCaffery*, 2008; *Bird and Kagan*, 2004; *Kagan and Jackson*, 2013; *Berryman et al.*, 2013], with potentially devastating regional shaking and tsunami. Overall, the seismic and tsunami hazards of the region have large uncertainties.

The locations of major and great earthquakes (magnitudes ≥ 7.0) along Tonga in the International Seismological Centre–Global Earthquake Model (ISC-GEM) Global Instrumental Earthquake Catalog (http://www.isc.ac.uk/iscgem/) [*Storchak et al.*, 2013], which extends back to 1900, are shown in Figure 1. None of the ISC-GEM
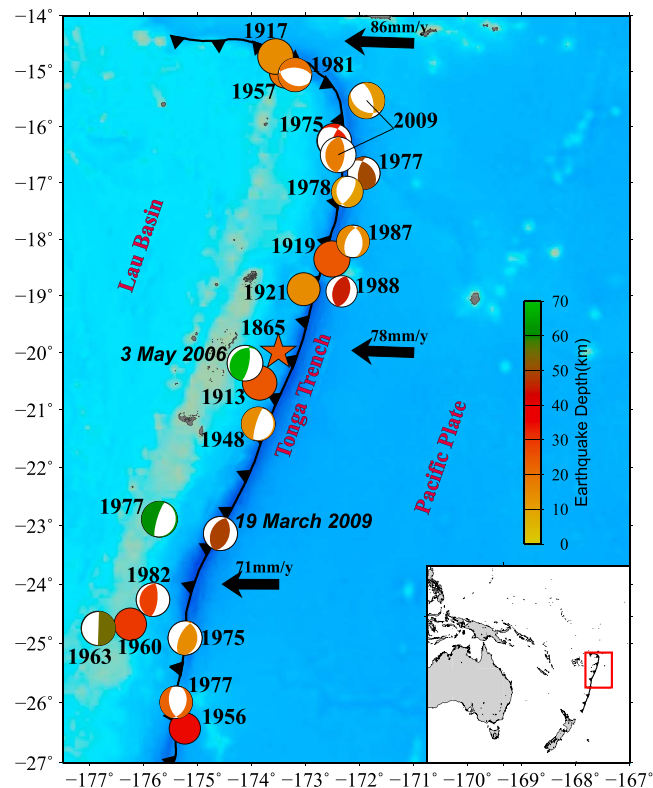
Figure 1. Large (magnitude ≥7) shallow (≤70 km deep) earthquakes in the Tonga subduction zone since 1900 (circles) from the ISC-GEM catalog. Mechanisms for the northern 1975 (−16.3°) and 1948 events are from *Okal et al.* [2011]. The southern 1975 (−24.9°) focal mechanism is from *Christensen and Ruff* [1988]. Best double-couple focal mechanisms from the global centroid moment tensor catalog are shown for the events from 1976 to present. The red star is an estimate of the epicenter for the 1865 earthquake from *Okal et al.* [2004]. The toothed curve indicates the position of the trench. The black arrows indicate the plate motion directions and rates for the Pacific plate relative to a fixed Australian plate from model MORVEL [*DeMets et al.*, 2010]. Back-arc spreading of the Lau Basin increases the trench convergence rate to about 240 mm/yr near −16°. Inset shows the location of the Tonga subduction zone.

magnitudes exceed 8.1, the value for the 30 April 1919 and 29 September 2009 events, although *Gutenberg and Richter* [1954] list M_S values of 8.7 for the 26 June 1917 Samoa event and 8.4 for the 30 April 1919 event. *Okal* [1992] estimated seismic moments from M_m values for the latter two events that predict lower M_w values of 8.0 and 8.2, respectively. An estimate of the epicenter of an additional event in southern Tonga on 17 November 1865 is included in Figure 1, and this may have been as large as M_w 8.3, but has very uncertain location and mechanism [*Okal et al.*, 2004].

Pacheco and Sykes [1992] analyzed earthquakes that occurred between 1900 and 1989 and found that only three of 19 major events in the Tonga region could be conclusively associated with thrust faulting. Available focal mechanisms are shown in Figure 1; for events after 1976 these are primarily from the global centroid moment tensor (GCMT) catalog (http://www.globalcmt.org), supplemented by mechanisms for the 26 December 1975 (M_w 7.7) and 8 September 1948 (M 7.5) events from *Okal et al.* [2011], the 11 October 1975 (M_w 7.6) event from *Christensen and Ruff* [1988], and the 11 December 1963 (M_w 7.6) event from *Isacks et al.* [1969]. The 29 September 2009 Samoa (M_w 8.1) outer rise normal faulting earthquake triggered nearby megathrust faulting with a total $M_w \sim 8.0$ [*Lay et al.*, 2010;

Beavan et al., 2010], for which a separate mechanism is included in Figure 1. The 26 June 1917 ($M \sim 8$) earthquake has uncertain mechanism but is not an underthrusting event and most likely involved intraplate deformation of the Pacific plate at the northern end of the subduction zone [e.g., *Okal et al.*, 2011]. The 30 April 1919 ($M \sim 8.1$ to 8.2) faulting mechanism is also not resolved, but *Okal et al.* [2011] suggest that the faulting may be intraplate based on their relocation of the event.

Two recent large compressional faulting earthquakes have struck in the Tonga subduction zone (Figure 2). The 3 May 2006 M_w 8.0 earthquake occurred in the vicinity of the megathrust and produced a small tsunami observed throughout the Pacific basin. The faulting geometry and tsunami excitation, along with an ISC-GEM hypocentral depth estimate of 15 km, suggest the possibility that this event was on the plate boundary. But the GCMT centroid depth is deeper than expected for megathrust faulting. We seek to establish whether this earthquake ruptured within the downgoing slab or possibly involved compound rupture including interplate slip. Another large compressional event occurred on 19 March 2009 (M_w 7.6) with a GCMT centroid depth that indicates rupture within the Pacific plate beneath the trench. Confirming that this is an intraplate event will also be addressed.

Quantifying these recent large compressional earthquakes is important for our understanding of seismic coupling and tsunami risk along the Tonga subduction zone. We analyze the 3 May 2006 event using teleseismic signals along with nearby GPS measurements of coseismic ground motions and aftershock locations from
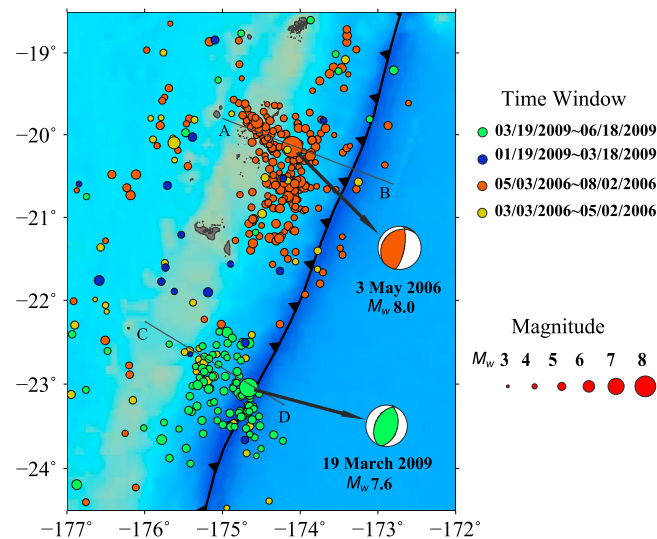
Figure 2. GCMT focal mechanisms and USGS-NEIC catalog locations of seismicity (circles) near the 3 May 2006 and 19 March 2009 large compressional faulting earthquakes in southern Tonga. Foreshock and aftershock activity is color-coded, and symbol sizes are scaled proportional to event magnitude (inset). The trench is indicated by the toothed curve. Line segments A-B and C-D indicate the locations of vertical sections showing seismicity depth distributions in Figures S1 and S6, respectively.

a temporary array of seismometers deployed on the Tonga Islands a few weeks after the main shock. Only teleseismic data are used to study the 19 March 2009 event, as we do not have local observations.

2. The 3 May 2006 Sequence

On 3 May 2006, a large compressional faulting earthquake (U.S. Geological Survey–National Earthquake Information Center (USGS-NEIC) parameters $m_b = 7.2$, $M_S = 7.9$; hypocenter: 20.187°S, 174.123°W, 55 km deep; 15:26:40 UTC; http://earthquake.usgs.gov/earthquakes/) occurred west of the Tonga trench in the vicinity of the megathrust (Figure 2). Tsunami with peak-to-trough amplitudes of about 0.5 m were observed in American Samoa, New Caledonia, Vanuatu, Hawaii, and California (USGS-NEIC) [*Tang et al.*, 2008]. The GCMT solution centroid location is 20.39°S, 173.47°W, at a depth of 67.8 km, with almost a purely double-couple solution (plane 1: strike = 226°, dip = 22°, rake = 123°; plane 2: strike = 11°, dip = 72°, rake = 78°) and a centroid time shift of 23.4 s. The GCMT seismic moment is 1.12×10^{21} Nm (M_w 8.0).

Given the importance of the source depth, we apply W-phase inversion [*Kanamori and Rivera*, 2008] to 170 three-component ground motion records filtered with a 1.5–5.0 mHz passband to estimate point-source parameters for source depths ranging from 10 to 120 km (Figure 3). The W-phase residual misfit curve (shown by red focal mechanisms indicating the solution found at each depth in Figure 3a) favors a centroid depth of ~60.5 km, which is the same as reported by *Duputel et al.* [2012]. In addition, because fundamental mode Rayleigh waves are more sensitive to earthquake centroid depth than the W-phase signals, we use the W-phase solution at each depth to predict the vertical component of Rayleigh waves in the same passband (arrivals between the second red dot and the green dot in Figure 3c). The Rayleigh wave residual misfit curve (Figure 3b) indicates a source depth of around 70 km, similar to the GCMT centroid depth. The long-period signals, thus, indicate that the main seismic radiation during the 3 May 2006 Tonga main shock occurred near 65 km depth. This depth is larger than found for interplate thrust events in other subduction zones, especially in island arcs.

2.1. Aftershock Sequence Characterization

We study the aftershock locations using a combination of teleseismic arrival times and data from seven portable seismic stations that we deployed on islands along the Tonga archipelago shortly after the earthquake (Figure 4 and Table 1). One station had a broadband response, and the other six were equipped with semibroadband Guralp CMG-40 T sensors (Table 1). Data from three permanent stations jointly operated by the Tongan government and the National Research Institute for Earth Science and Disaster Prevention (NIED) in Japan were also used. These consisted of two broadband stations, TPU and VAV, and one with a short-period seismograph, HAP (Figure 4 and Table 1). The temporary stations operated continuously for 4 months from June to mid-October 2006 (Table 1). Due to the remote location and logistical difficulties associated with working in the Tonga archipelago, the first temporary station was deployed on 3 June and the array was completed on 19 June, 47 days after the main shock (Table 1).

Initial event detection was performed using a short-term average/long-term average detection algorithm, and subsequently, P and S phases were picked visually. We isolate aftershocks during June and July that
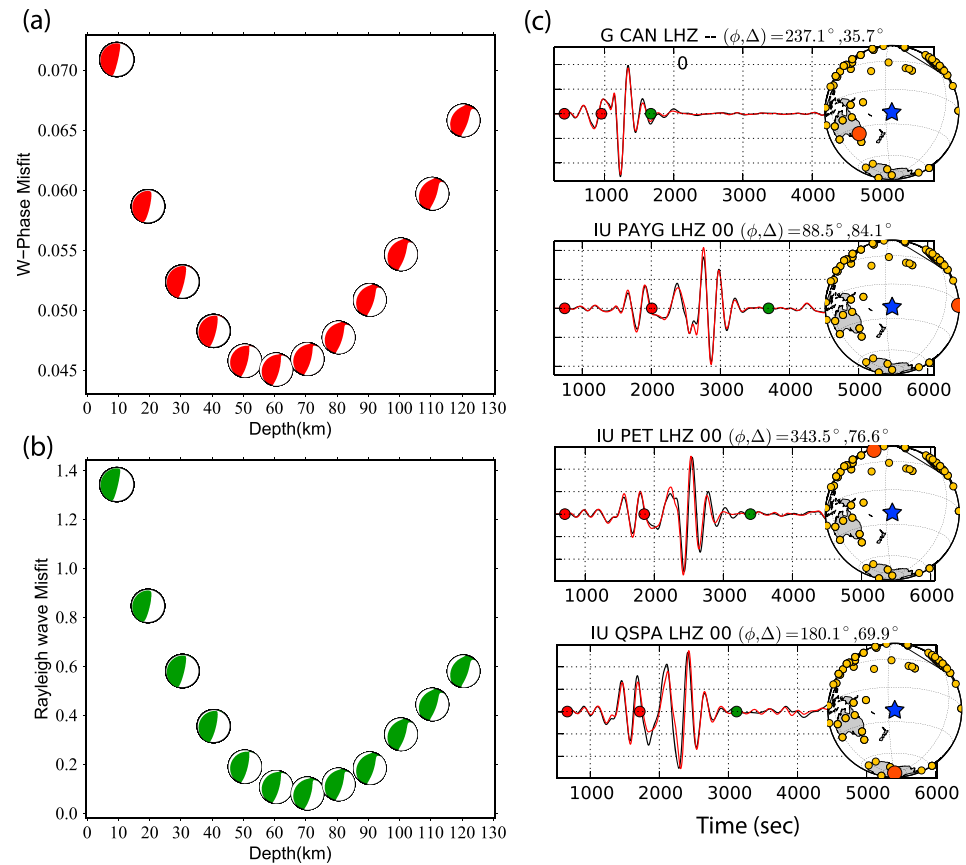
Figure 3. Residual waveform misfit for ground displacements in the 1.5–5.0 mHz frequency range versus point-source depth for (a) W-phase inversions (red focal mechanisms for each depth) and for (b) observed and predicted Rayleigh wave signals using the W-phase solution at each depth (green focal mechanisms) for the 3 May 2006 Tonga event. (c) Example observed (red lines) and synthetic (black line) waveforms are shown. The time window between the red dots is used for the W-phase inversions, and the time window between the second red dot and green dot is used for predicted Rayleigh wave misfit calculation. The gold dots on the maps are the positions of all stations used in the inversion with the red dot indicating the position of the specific station shown. The blue star indicates the source epicenter.

are distinct in location and timing from the other seismicity detected during the study period. We relocate all well-constrained aftershocks using the joint hypocentroidal decomposition method [*Jordan and Sverdrup*, 1981] and a local 1-D velocity structure estimated from *Crawford et al.* [2003] for the crust and Preliminary Reference Earth Model (PREM) [*Dziewonski and Anderson*, 1981] for the mantle. Teleseismic travel times were calculated with the International Association of Seismology and Physics of the Earth's Interior 91 velocity structure [*Kennett and Engdahl*, 1991].

We limit our analysis to those aftershocks that have more than 10 arrivals and a maximum 95% confidence ellipsoid semiaxis length of less than 20 km. In addition to locally detected events, we utilize arrival data from the International Seismological Centre (ISC; http://www.isc.ac.uk) for the main shock and for a number of aftershocks (Table 2) that were also detected locally by the permanent network and for which there are GCMT solutions. Prior to the temporary deployment (3 May 2006 to 4 June 2006) there were only the three permanent stations operating in Tonga. These did not provide enough data to obtain good earthquake locations on their own, so we only pick local arrivals from events for which there was an origin based on teleseismic arrival data and relocate those events using the combined local and teleseismic data.

In all, we relocated the main shock and 335 aftershocks, 287 having only local data and 48 having both local and teleseismic arrivals. Twenty three of the relocated events have GCMT solutions (Table 2). We find the main shock hypocentral depth to be 70.7 ± 3.5 km to 2 standard deviations. This can be compared with the hypocentral depth estimates of USGS-NEIC (55 km) and ISC (53.5 km) and the 60.5–70 km centroid depths
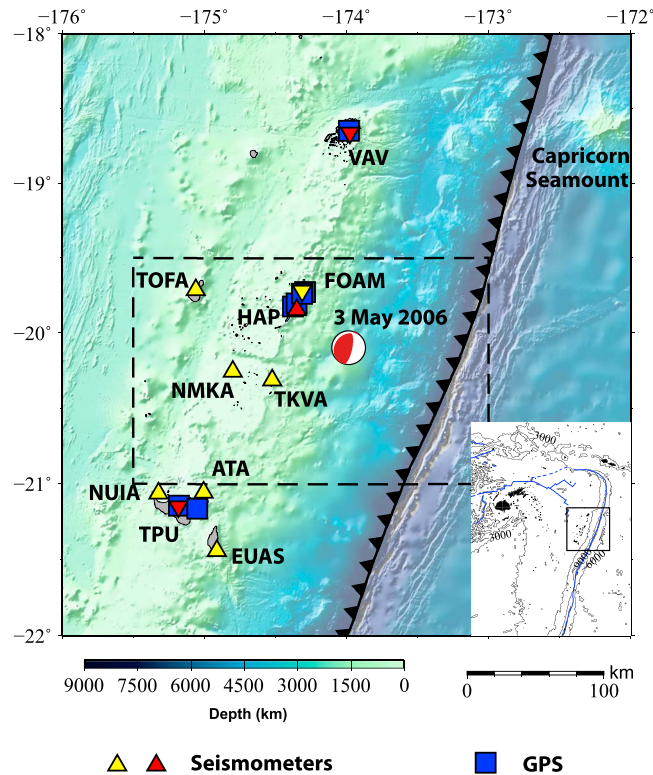
Figure 4. Map of regional seismic station locations with upright triangles and inverted triangles representing temporary and permanent stations, respectively. Broadband stations are red, and semibroadband and short-period stations are yellow. GPS stations are labeled with blue squares. Station names (Table 1) and the Capricorn Seamount are labeled. The trench axis is denoted by a heavy, toothed black line. The region of Figure 5 is outlined in dashed rectangle, and the main shock focal mechanism from the GCMT catalog is plotted at the relocated hypocentral position. Color scale is for bathymetry. Inset: regional setting of the network. Study region is outlined in black, and the blue line denotes plate boundaries. The 2500 m bathymetric contours are plotted to denote major structural features.

from long-period moment tensor inversions. The average uncertainty of the earthquake locations (here considered to be the mean of the three semiaxes of the 95% confidence ellipsoids) is 6.2 km with a standard deviation of 2.5 km.

A vertical cross section through the relocated events indicates a dipping plane of seismicity that projects to the trench axis that we interpret as the interplate megathrust (Figure 5b). This is about 10 km shallower than predicted for the Slab 1.0 model of *Hayes et al.* [2012], as seen in Figure 5b, but that model does not have the local network constraints of our aftershock locations. Only a few of the GCMT focal mechanisms for aftershocks indicate plausible thrust faulting located on the megathrust, but the overall distribution would be hard to relate to an upper plate fault in the island arc as it extends into the mantle. The main shock nucleation occurred about 30–40 km beneath the shallow seismic zone, and the long-period centroid depths are similar to the hypocentral depth, suggesting bilateral or circular rupture expansion. Very few aftershocks locate near the main shock hypocenter, none of which are large enough to have GCMT solutions, so it is not possible to use the aftershock distribution to confidently identify the fault plane between the two possibilities (dashed lines) in Figure 5b. Given the absence of seismicity on the shallow-dipping rupture plane option and the clear lineation of seismicity at shallower depth, we interpret the main shock as being intraplate, 30–40 km below the interplate thrust zone. Forcing the main shock location to lie on the plate boundary would

Table 1. Location of Local Seismic Stations in Tonga and Dates of Operation[a]

Station	Latitude	Longitude	Type	On Date	Off Date
EUAS	−21.44	−174.91	SBB	06 Jun 2006	11 Oct 2006
TPU*	−21.15	−175.18	BB	-	-
NUIA	−21.06	−175.32	SBB	03 Jun 2006	13 Oct 2006
ATA	−21.06	−175.00	SBB	19 Jun 2006	12 Oct 2006
TKVA	−20.32	−174.52	SBB	11 Jun 2006	16 Oct 2006
NMKA	−20.26	−174.80	SBB	09 Jun 2006	16 Oct 2006
HAP*	−19.83	−174.35	SP	-	-
FOAM	−19.74	−174.29	BB	12 Jun 2006	14 Oct 2006
TOFA	−19.71	−175.06	SBB	14 Jun 2006	17 Oct 2006
VAV*	−18.66	−173.98	BB	-	-

[a]Stations that are part of the permanent network are denoted by an asterisk. Station types: SBB: Guralp 40-T sensor, BB: broadband seismometer, SP: short-period seismometer. On/off dates for temporary network stations denote installation/removal.

Table 2. Summary of Relocated CMTs During the Study Period for Which Local Arrival Data Exist[a]

Event Number	Date	Origin Time	Latitude °N	Longitude °E	Depth (km)	M_w	M_l	Arrivals	Relative Uncertainty (km)
1	03 May 2006	15:26:41	−20.10	−173.99	70.71	8.0	7.5	303	3.4
2	04 May 2006	11:25:27	−20.64	−173.75	16.39	5.9	5.6	196	5.7
3	05 May 2006	04:19:43	−20.25	−173.68	27.75	5.5	5.8	205	4.2
4	05 May 2006	05:33:25	−19.92	−173.44	19.54	5.2	5.6	113	4.7
5	05 May 2006	06:16:18	−19.84	−174.34	21.07	5.9	6.6	174	3.8
6	05 May 2006	08:49:08	−19.92	−173.71	24.94	5.1	4.8	63	8.2
7	07 May 2006	02:33:47	−20.10	−174.15	39.12	5.6	5.3	170	4.6
8	07 May 2006	12:30:33	−20.05	−173.82	38.24	4.9	5.0	75	6.1
9	07 May 2006	22:06:25	−20.12	−173.75	39.74	4.9	4.7	49	8.0
10	09 May 2006	10:27:52	−19.87	−174.28	7.36	5.1	6.0	75	6.0
11	14 May 2006	04:54:15	−20.11	−174.27	42.22	5.0	5.6	77	4.9
12	16 May 2006	20:55:49	−20.71	−173.83	21.03	5.7	5.6	169	4.8
13	17 May 2006	03:06:17	−20.66	−173.76	16.00	5.8	6.3	193	4.2
14	17 May 2006	21:57:50	−20.70	−173.74	16.90	5.5	6.2	142	4.4
15	28 May 2006	03:36:19	−19.93	−174.26	54.22	5.7	6.2	218	3.8
16	01 Jun 2006	22:31:27	−20.16	−173.56	29.24	4.9	5.0	159	5.7
17	02 Jun 2006	01:28:26	−20.17	−173.50	19.78	5.1	5.1	211	5.0
18	02 Jun 2006	06:59:42	−20.12	−173.55	29.48	5.2	4.8	102	4.8
19	03 Jun 2006	13:26:54	−20.97	−173.83	23.54	5.1	5.1	53	7.0
20	03 Jun 2006	15:27:51	−20.55	−174.10	25.64	5.2	5.2	187	4.9
21	17 Jun 2006	03:45:59	−20.04	−174.21	68.74	4.9	5.2	182	3.1
22	28 Jun 2006	13:00:30	−20.80	−173.82	45.65	5.0	4.9	49	4.9
23	05 Jul 2006	03:44:10	−20.58	−173.83	20.53	5.6	6.0	257	3.1

[a]M_w is from CMT solution, and M_l is from P-S amplitude ratio recorded by local array. Origin information is the final location, arrivals include both teleseismic arrivals from ISC and local arrivals recorded by temporary and permanent arrays in Tonga, and uncertainty is the average of the three semiaxes for the 95% uncertainty ellipsoid. Event number corresponds to CMT plotted in Figure 5.

require a very steep kink in the interface and would give a dip much larger than that of the shallowly dipping nodal plane. It would also require that the deepest ever recorded great interplate thrusting occurred in an island arc environment. We do not think this is at all likely.

There are three regions of significant seismicity following the main shock: on what we interpret to be the plate interface downdip of the main shock, a lobe of updip seismicity extending north-northeast of the main shock, and another lobe that extends south-southeast (Figure 5a). The majority of the teleseismically detected aftershocks occurred prior to the temporary deployment located updip of the main shock. As we have not found any strong correlation between earthquake timing and location, the entire aftershock region appears to have quickly activated following the main shock.

The downdip aftershock region on the shallow thrust zone extends to about 55 km depth, which we believe corresponds to the downdip limit of the seismogenic zone of the plate boundary. We also carried out a relative location of all the GCMT earthquakes that precede the main shock (not shown). We found that moderate size earthquakes with thrust faulting GCMT solutions that preceded the main shock have large depth uncertainties but locate eastward from the main shock in the shallow part of the thrust zone and not in the downdip region of high aftershock activity. The downdip aftershocks may have been driven by stress changes imparted by the intraplate faulting, possibly in regions of conditional stability, or there may have been coseismic slip triggered on the megathrust during the main shock. We will explore these two possibilities below.

The updip seismicity is more widely distributed along trench strike than is the downdip activity. The two lobes are apparent for both locally and teleseismically located aftershocks. The updip focal mechanisms are variable, indicating complex intraplate deformation. Eight focal mechanisms involve normal faulting (Figure 5), which is rare among GCMT mechanisms in the updip region prior to the main shock. Most of the normal faulting solutions are within 20 km of the plate interface. The slab has significant curvature in this region, so that bending stresses should produce near-horizontal extensional stress in the upper part of the shallow slab. We interpret this diffuse extensional faulting as resulting from stress changes caused by the main shock, possibly including any triggered coseismic or afterslip in the region of downdip aftershocks. The normal faulting may then indicate stress modulation of the shallow slab by the deeper stress
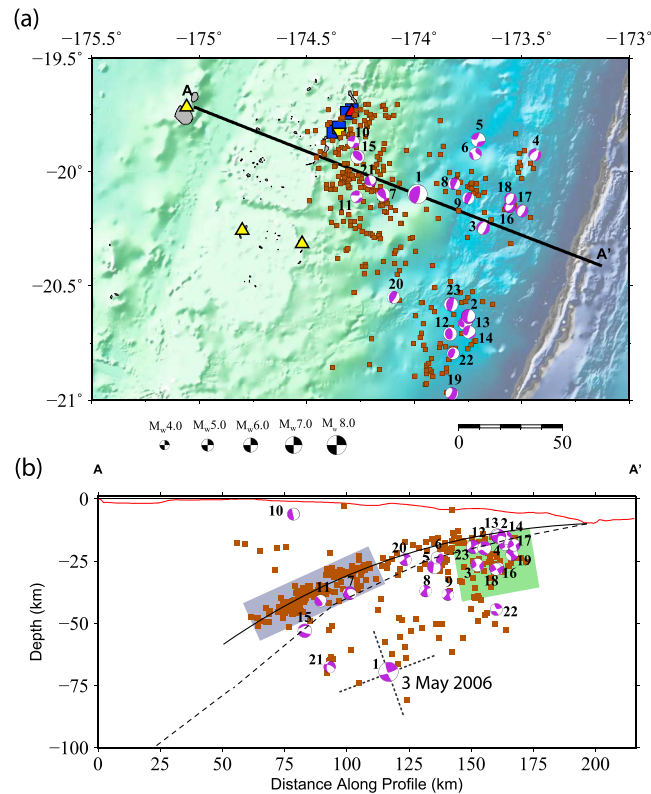
Figure 5. (a) Map and (b) vertical cross section of relocated 3 May 2006 main shock (1) and aftershocks, including those with GCMT focal mechanisms (numbered as in Table 2). Locally detected earthquakes are brown, and locally detected events with GCMT faulting mechanisms are violet. The heavy black line AA′ locates the vertical cross section below. Two lobes of updip seismicity are apparent in the map view. The bathymetric scale is the same as in Figure 4. The cross section has tectonic interpretations. Bathymetry is indicated in red. Dotted black lines—possible fault plane geometries for the main shock; black line—interpreted slab interface; dashed black line—depth below surface of the slab interface from model Slab 1.0 [Hayes et al., 2012]; blue rectangle—zone of thrust faulting along the megathrust zone; green rectangle—zone of intraplate horizontal tension.

release cycle, as observed for many large megathrust ruptures [Ammon et al., 2008; Christensen and Ruff, 1988; Dmowska et al., 1988].

2.2. Main Shock Fault Positioning and Rupture Process

We invert for the finite-fault slip distribution of the 3 May 2006 main shock using 113 teleseismic P and SH wave ground displacement recordings in the period range of 1 to 200 s from global broadband seismic stations, along with eight static displacements from three continuous GPS stations (TONG, VAVS, and NIUM) and five campaign GPS stations (HAKM, LFKA, FOA5, FOA7, and PAST) in the Tonga region (Figures 4 and 10; see also Table 3). For the three continuous GPS stations, 1 week data from just before and just after the earthquake were used. For the campaign stations, we needed to rely on the difference between measurements made 1.5–2.5 years prior to the earthquake and about 3 weeks after the event (see Table 3). Daily solutions were produced for all stations of the Australia-South Pacific GPS network using Bernese 5.0 software [Dach et al., 2007]. The daily solutions were aligned to the International Terrestrial Reference Frame 2005 reference frame [Altamimi et al., 2007]. If more than one daily solution was available before or after the earthquake, they were combined so as to have one solution before and one after

the earthquake. To take plate motions into account, horizontal solutions for the campaign sites were projected to the day just before or the day just after the earthquake using the Tonga plate model [Bird, 2003]. Vertical solutions for the campaign sites were not impacted significantly by the plate motions so that no projection was needed for them. Displacements were calculated by differencing the solutions obtained for the time just after earthquake

Table 3. GPS Measurements of Coseismic Displacements Caused by 3 May 2006 Earthquake[a]

				Displacements and Their Uncertainties (mm)		
Site Name	Longitude	Latitude	Measurement Times	North	East	Up
TONG	−175.179	−21.144	Continuous	25 ± 3	67 ± 3	−10 ± 6
VAVS	−173.983	−18.650	Continuous	−36.3 ± 3	24 ± 3	−3 ± 6
NIUM	−169.927	−19.077	Continuous	5 ± 3	−9 ± 3	0 ± 6
HAKM	−175.049	−21.164	7–10 Dec 2004 to 20–28 May 2006	32 ± 5	57 ± 5	−16 ± 12
LFKA	−174.377	−19.824	7–10 Dec 2004 to 21–22 May 2006	−221 + 6	373 ± 6	−201 ± 13
FOA5	−174.292	−19.728	31 Jan 2003 to 23 May 2006	−247 ± 15	309 ± 15	−203 ± 27
FOA7	−174.314	−19.740	3 Feb 2003 to 24 May 2006	−246 ± 15	316 ± 15	−199 ± 27
PAST	−174.351	−19.805	24 Jan 2003 to 25 May 2006	−259 ± 15	336 ± 21	−206 ± 30

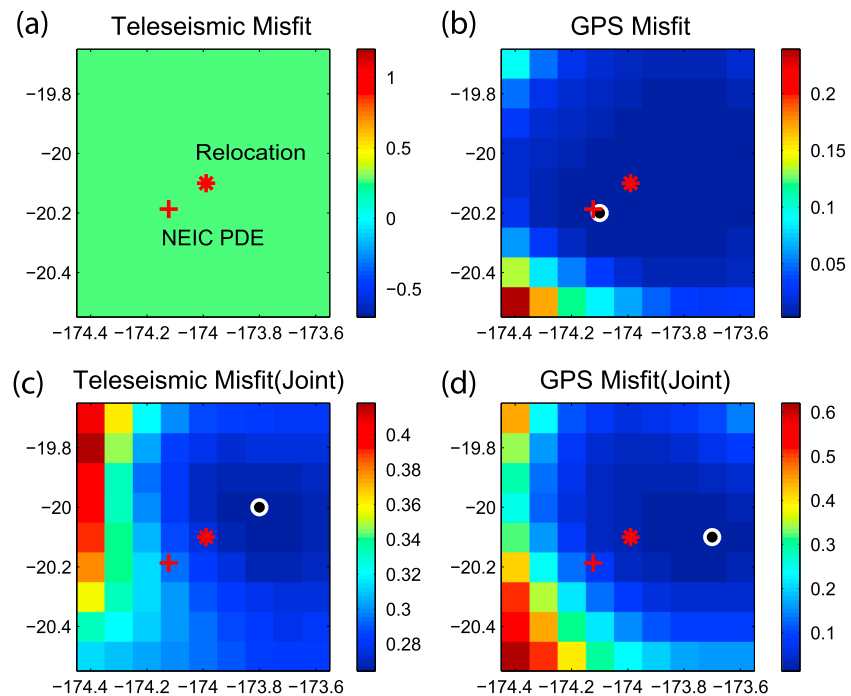[a]Measurement times, displacements, and their uncertainties (95% probability) are indicated.

Figure 6. Residual waveform misfit distributions for a 65 km deep grid of hypocentral locations for the 3 May 2006 Tonga main shock using the shallowly dipping fault plane, for (a) teleseismic body wave inversion misfits, (b) local GPS static offset inversion misfits (station locations are shown in Figure 4), (c) teleseismic body wave misfits for joint inversion of teleseismic and GPS data, and (d) GPS static offset misfits for joint inversion of teleseismic and GPS data. The white circles indicate the minimum misfit position for each case. The final preferred hypocenter is an average of these, located at −173.8°E, −20.1°N, about 30 km east-northeast from the USGS/NEIC location (red plus signs) and 20 km east of the locally relocated hypocenter (red asterisks).

with that obtained for a time just before the earthquake. For the continuous GPS sites, uncertainties of the displacements were calculated by propagating the GPS solution uncertainties. For the campaign GPS sites, uncertainties of the displacements were calculated by propagating the GPS solution uncertainties and adding to these the plate motion projection uncertainties. The displacements and their uncertainties are listed in Table 3.

We use a kinematic linear least squares inversion with positivity constraint for a specified fault geometry, constant rupture expansion velocity, variable subfault rake, and subfault source time functions parameterized by several overlapping triangles, developed by *Hartzell and Heaton* [1983] and *Kikuchi and Kanamori* [1991] and modified for joint inversion by *Yue et al.* [2014]. Green's functions for a regional velocity model based on CRUST 1.0 [*Laske et al.*, 2013] are computed for the teleseismic *P* and *SH* waves using the reflectivity method of *Kikuchi and Kanamori* [1991] and for the local static displacements by the method of *Wang et al.* [2003].

We initially used the hypocentral parameters from the USGS-NEIC and fault plane orientations given by the best double-couple mechanism from the GCMT inversion. These assumptions allow the seismic and geodetic data to be quite well modeled for the shallowly dipping plane (strike 226°, dip 22°), but the fit to the local GPS displacements was very poor for the steeply dipping plane (strike 11°, dip 72°). The misfit for the steeply dipping plane could not be eliminated by modest changes in focal mechanism or rupture velocity. However, the GPS stations have limited azimuthal coverage, with the four closest stations being about 50 km west of the hypocenter (Figure 4) and other stations being further to the north, southwest, and east. This configuration makes the precise location of the fault very important for modeling the GPS data, and it is likely that absolute locations in this region are biased toward the slab dip direction (WNW) by high-velocity slab structure and the sparse southern hemisphere seismic station coverage. This concern is supported by the relocation using the three local *P* arrival times, which gives an eastward shifted hypocenter at 20.10°S, 173.99°W at 70.7 km depth (Table 2). The hypocenter could locate at shallower depth somewhat further to the east and still match the local
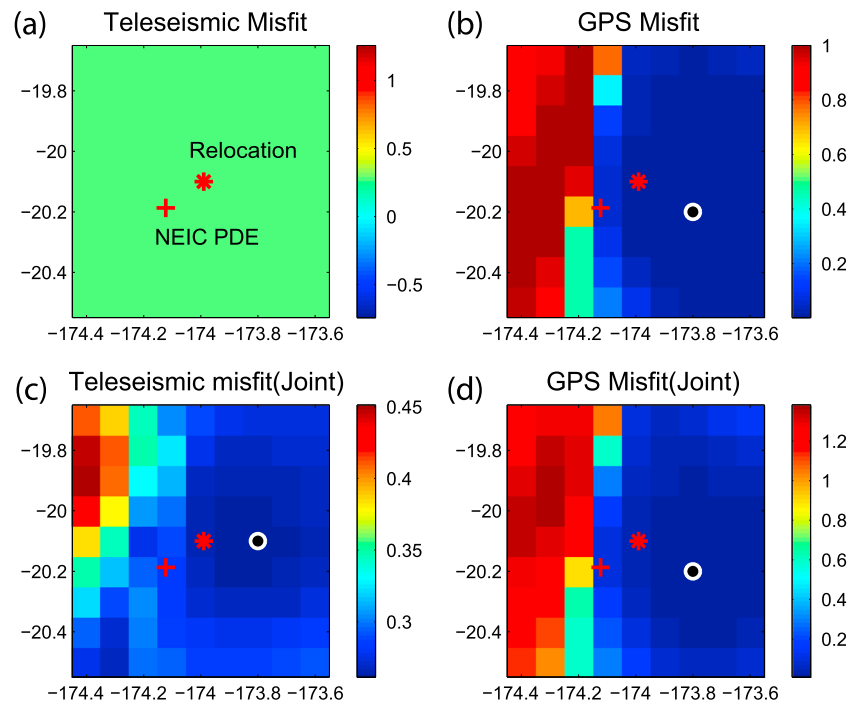
Figure 7. Residual waveform misfit distributions for a 65 km deep grid of hypocentral locations for the 3 May 2006 Tonga main shock for the steeply dipping fault plane showing (a) teleseismic body wave inversion misfits, (b) local GPS static offset inversion misfits (station locations are shown in Figure 10), (c) teleseismic body wave misfits for joint inversion of teleseismic and GPS data, and (d) GPS static offset misfits for joint inversion of teleseismic and GPS data. The white circles indicate the locations that give minimum residuals for the separate data sets in the joint inversions, relative to the USGS/NEIC location (red plus signs) and the locally relocated hypocenter (red asterisks).

and teleseismic arrival time data. We found that small shifts of the hypocenter (and hence, the overall placement of the fault model relative to the GPS network) could allow the steeply dipping fault plane to give a fit to the combined teleseismic and static offset data sets comparable to that for the shallowly dipping fault plane, so we searched over a range of possible fault placement positions.

Figure 6 shows the 9×9 grid of hypocentral positions considered, with the NEIC epicenter indicated by red plus signs and the epicenter that included local travel times indicated by red asterisks. We performed inversions of just the teleseismic data, just the GPS data, and the combined data for hypocentral depths of 60, 65, and 70 km. Figure 6 shows the resulting waveform misfit of inversions for a hypocentral depth of 65 km at each grid position for the shallowly dipping fault plane. The residual misfit for teleseismic-only inversion provides no resolution of absolute hypocenter location because the data and synthetics are aligned in the inversion process to suppress path propagation errors. The GPS-only inversions also have little variation with the hypocenter until quite large westward shifts are considered and result in rapid degradation of fit. The residual misfit of joint teleseismic and GPS static offset inversion does improve with the shift from the NEIC location to the locally relocated position but has minima for each data type for hypocenters somewhat further to the east (white circles). Our preferred 65 km deep hypocenter at −20.1°N and −173.8°E is about 30 km east-northeast of the NEIC hypocenter and 20 km east of the locally relocated hypocenter.

A search over hypocentral position using the steeply dipping fault plane model (Figure 7) yields similar results; 20–30 km eastward shifts improve the fit for the GPS-only and joint inversions, both of which are much more sensitive to the absolute fault placement than for the shallowly dipping fault models (note the large variations in residual amplitudes relative to Figure 6). Given that the preferred hypocentral locations are similar for the two-fault plane choices, we use the preferred hypocenter for the shallowly dipping fault plane in our final models. We view the shift in hypocenter as being well within the actual uncertainty of the absolute hypocenter estimates.
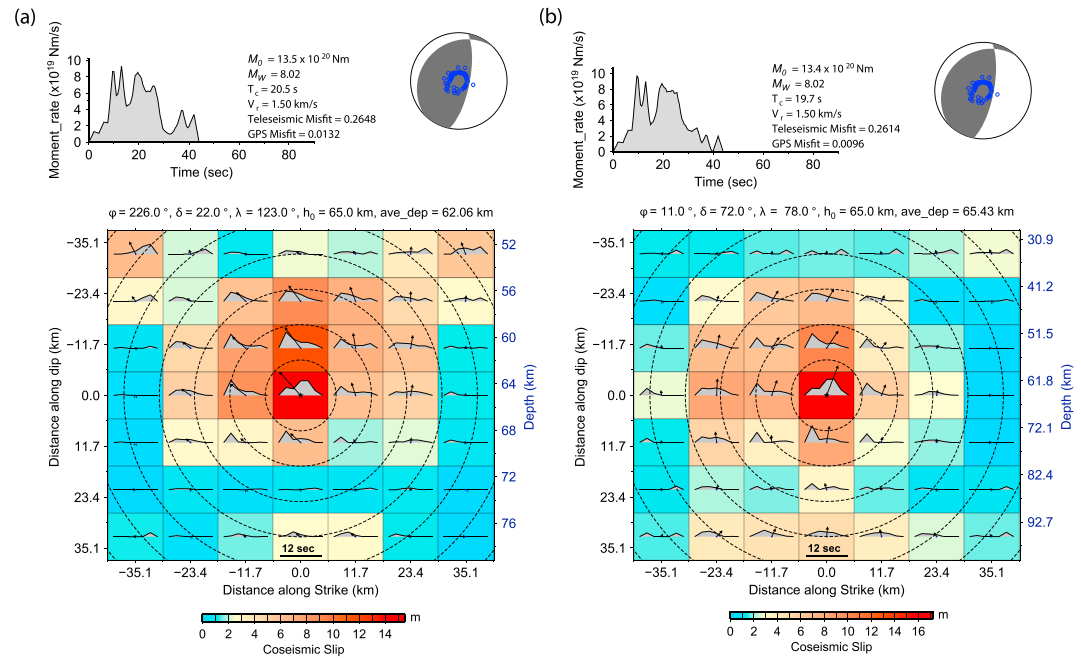
Figure 8. (bottom) Finite-fault slip distribution for the (a) shallowly dipping fault plane model and (b) steeply dipping fault plane model of the 3 May 2006 Tonga event from joint inversion of teleseismic body waves (*P* and *SH*) and static offsets (GPS locations are shown in Figure 10). Vectors in each subfault indicate the average subfault rake and slip magnitude, which is also color-coded. (top) The moment rate function and lower hemisphere focal mechanism with *P* wave sampling points are shown. Rupture expansion velocity is 1.5 km/s, with the rupture front indicated by dashed circles at 5 s intervals. The hypocenter is at −173.8°E, −20.1°N and 65 km deep.

For the shallowly dipping fault geometry, Figure 8a shows a joint inversion of teleseismic and static offset data. The source time function, average focal mechanism, and finite-fault slip distribution are shown using the preferred hypocenter. We use the GCMT fault geometry with strike 226° and dip 22°, allowing variable rake, and find an average rake of 125.3° (the GCMT point-source value is 123°). The model dimensions are 81.7 km × 75.8 km, comprised of 7 × 7 subfaults. Each subfault source time function is parameterized with five symmetric triangles with 2 s risetime lagged by 2 s, giving possible total subfault durations of 12 s. A rupture expansion velocity of 1.5 km/s is used. This value is not well constrained, but the main slip zone of the rupture does appear to be quite compact, so longer subfault rupture durations are required for higher expansion velocities, increasing the number of model parameters. The solution in Figure 8a is similar to the finite-fault inversion for a shallow-dipping fault model (strike 221°, dip 22°) posted on the USGS-NEIC website (http://earthquake.usgs.gov/earthquakes/eventpage/usp000eg5g#scientific_finitefault), which has an effective rupture expansion velocity of ~2 km/s.

The main slip patch has a length of ~50 km in the along-dip direction, with an average depth of slip of 62.3 km. The estimated seismic moment is 1.35×10^{21} Nm, which is 21% higher than the GCMT moment, despite using the latter in a penalty function, but this is strongly affected by the length of signal inverted. The source velocity model is from CRUST 1.0 and differs from PREM [*Dziewonski and Anderson*, 1981] used in the long-period modeling, and this is most important for the static displacement calculations, which may account for part of the difference.

One of the challenges in modeling the body waves for this event is that there are strong reverberations in the *P* coda for stations toward the northeast and along the steeply dipping *P* wave nodal plane (Figure S2 in the supporting information). These are also not well fit in the USGS-NEIC inversion. These appear to be water multiples that overlap the later portion of the source time function, so that only the first ~35 s of the rupture is well resolved. If long data time windows are used, strong late features appear at the shallow edge of the model, leading to overestimation of the moment. Complicated bathymetry may produce large water reverberations that are not well modeled with flat-lying bathymetry, particularly for events near deep ocean
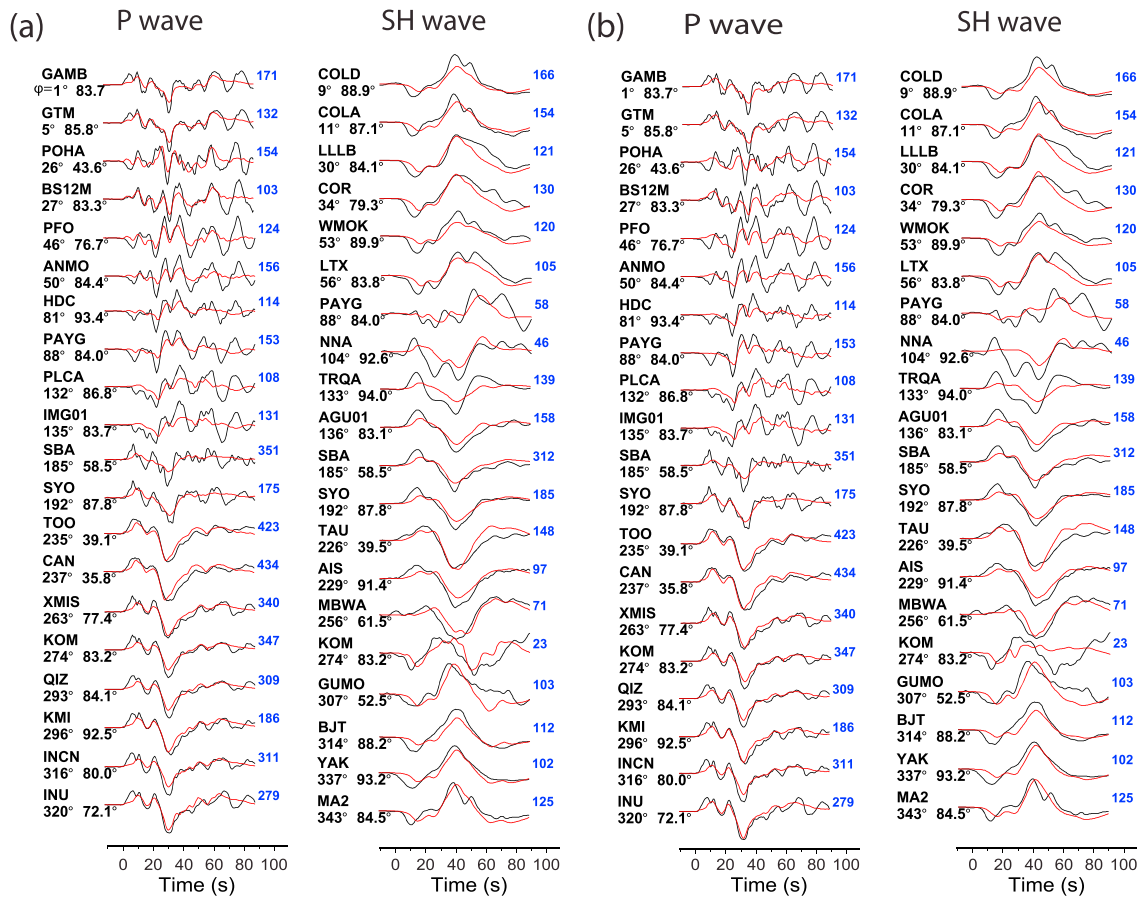
Figure 9. (a) A subset of observed (black) and predicted (red) teleseismic *P* and *SH* waveforms for the 3 May 2006 Tonga event for the joint inversion of teleseismic body waves and local static offsets for the shallowly dipping fault. The complete set of waveforms is shown in Figure S3. (b) The same subset of waveform comparisons for the joint inversion assuming the steeply dipping fault. The complete set of waveforms is shown in Figure S4.

trenches [e.g., *Wiens*, 1989; *Okamoto*, 1994]. Modeling the full three-dimensional effects of variable bathymetry is beyond the scope of this study, so we constrain the inversion to fit the main *P* wave pulse and *SH* phases to the extent viable with a single 1-D model. The centroid time for the inverted slip model is 20.5 s, slightly shorter than the 23.4 s GCMT centroid time, indicating that there is little, if any, missing later source energy release.

Figure 9a shows a subset of the observed *P* and *SH* waveforms (black) and synthetic seismograms (red) predicted by the inverted slip model on the shallowly dipping fault plane (Figure 8a). The overall fits are acceptable, but some initial *P* wave motions near the steep nodal plane are not well fit. No obvious improvement was found for perturbations of the fault orientation or other source parameters. All of the observed and modeled teleseismic body waves are shown in Figure S3. Figure 10 shows the local GPS-observed (white) and -predicted (red) static offsets for the model in Figure 8a. The static deformation observations are generally fit well, but there is some inconsistency in the horizontal displacement vector observations from nearby stations that delimits how well any model can match the data.

For the steeply dipping fault geometry, a finite-fault slip model for the preferred hypocenter is shown in Figure 8b. The fault dimensions and subfault parameterization are the same as for the model with a shallowly dipping plane. The corresponding observed and model teleseismic waveforms are shown in Figure 9b, where the misfit of some early *P* wave motions is seen to be somewhat more pronounced than for the shallow-dipping fault, notably at azimuths to the northeast, although the overall variance reduction is marginally higher. All of the observed and modeled teleseismic body waves are shown in Figure S4. The static offsets are quite well modeled (Figure S5), similar to the shallowly dipping fault case, as long as the preferred (shifted) hypocentral location is used. We again perturbed the fault dip and strike but did not find significant
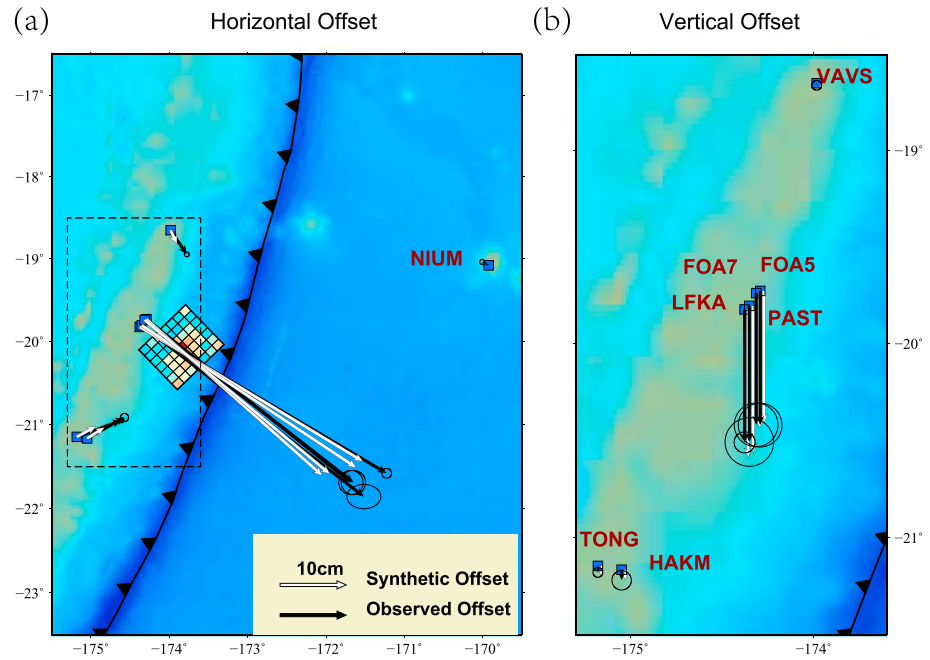
Figure 10. Locations of local GPS campaign stations (blue squares) that provide (a) horizontal (black vectors) and (b) vertical (black vectors) coseismic offsets, within which Figure 10b is a zoomed area of the dashed rectangle in Figure 10a, for the 3 May 2006 Tonga event. Their uncertainties (95% probability) are indicated by black ellipses. Predicted displacements for the shallowly dipping fault plane model in Figure 8a are shown by white vectors for horizontal motions (Figure 10a) and for vertical static offsets (Figure 10b).
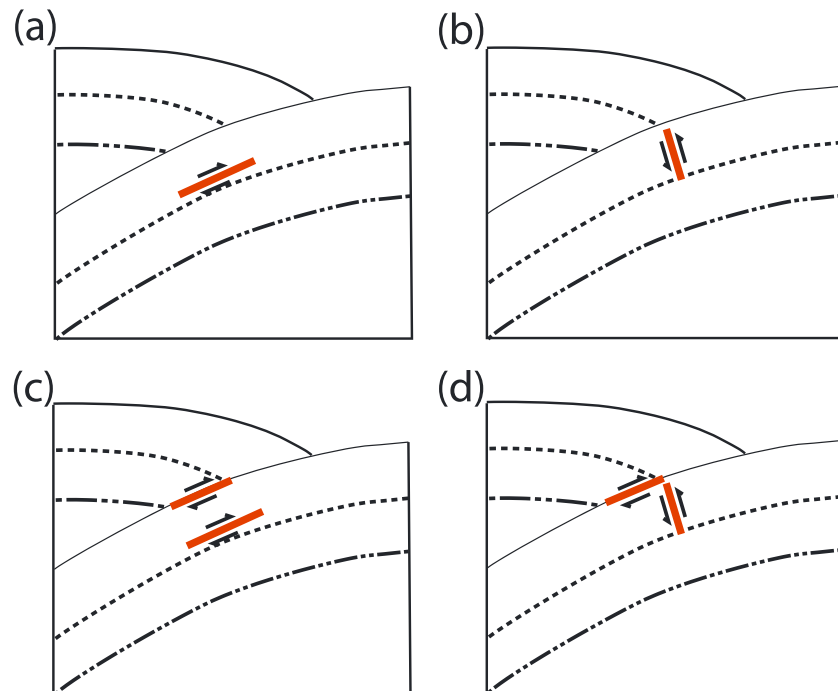
Figure 11. Rupture scenarios considered for the coseismic faulting process of the 3 May 2006 earthquake: (a) single shallowly dipping intraslab fault plane; (b) single steeply dipping intraslab fault plane; (c) two faults, with the megathrust fault triggered by rupture on the shallowly dipping intraslab plane; and (d) two faults, with the megathrust fault triggered by rupture on the steeply dipping intraslab fault plane.

improvement for different geometries. These inversions do not provide a clear preference for the actual rupture plane. Neither geometry would be considered typical of intraplate faulting below the megathrust and the diffuse aftershocks could be activated by dynamic triggering for either case, so the precise faulting is unresolved.

2.3. Multiple Fault Models

The relocated aftershock sequence (Figure 5) clearly indicates activity near the downdip and updip regions of the inferred megathrust that does not lie on either possible fault plane for the main shock (Figures 11a and 11b). This indicates triggered faulting off the main fault during the aftershock sequence, and the available aftershock focal mechanisms indicate that the updip region included activation of multiple normal faults. The downdip activity is more spatially concentrated and plausibly involves deformation on the megathrust. This may have included coseismic slip on the megathrust driven by the intraplate faulting, or just induced aftershock activity on the megathrust, perhaps associated with induced slow slip.

Initial intraplate rupture triggering interplate faulting in a single large event has been demonstrated in several cases, including the 29 September 2009 Samoa earthquake (M_w 8.1) [*Lay et al.*, 2010] and the 4 June 2000 Sumatra earthquake (M_w 7.9) [*Abercrombie et al.*, 2003]. In those cases the intraplate events were very different in faulting orientation (normal and strike-slip faults, respectively) from the triggered megathrust faulting, leading to nondouble-couple point-source moment tensors and complex waveforms that could not be fully modeled using a single fault. The situation for the 3 May 2006 Tonga event is more difficult to resolve. Given that the intraplate primary faulting focal mechanism is not very different from an interplate focal mechanism, any coseismic slip on two faults would have a point-source moment tensor solution with little nondouble-couple component allowing the overall motions to be well matched using a single fault as shown above.

We explored the possibility of coseismic slip on the downdip portion of the megathrust using two-fault scenarios having an interplate thrust event dynamically triggered by either shallowly dipping or steeply dipping intraslab main shocks (Figures 11c and 11d). We assume that the waveforms of any "triggered" interplate subevent interfere with waveforms generated by the intraslab main shock but otherwise lack any specific constraint on relative timing or kinematic parameters of the hypothesized triggered rupture. Many joint inversion models were run with finite-fault parameterizations of the intraslab and interplate geometries with varying hypocenters of the subevents or changing the initiation time of the induced interplate event. We did not find a satisfactory two-fault model that can fit the teleseismic body waves and static offsets significantly better than when using a single shallowly dipping or steeply dipping fault. Most solutions concentrate slip on the intraplate fault with any slip on the interplate fault occurring later and overlapping the onset of water reverberations. Of course, not all possible models could be considered, and it is clear that use of 1-D Green's functions is not sufficient for accounting for water multiples at all azimuths. Thus, we cannot rule out the possibility of some megathrust slip having been triggered coseismically, but from a parsimonious perspective we prefer a single-fault model for the main shock faulting and attribute the aftershocks to delayed off-fault triggering.

2.4. Coulomb Stress Changes and Triggering

Thinking qualitatively about the multiple fault scenarios in Figures 11c and 11d, the shallowly dipping intraplate faulting has slip that would reduce driving stress of the megathrust above it, whereas the steeply dipping intraplate faulting may tend to reduce normal stress in the deeper megathrust. While coseismic rupture of the downdip megathrust could be dynamically triggered by strong stress oscillations for either geometry, static stress changes may play an important role for the aftershock sequence. We use Coulomb 3 software [*Toda et al.*, 2011] to compute the Coulomb stress changes for thrusting on the megathrust plate interface for the slip distributions on both shallowly dipping (Figure 12a) and steeply dipping (Figure 12b) intraslab fault geometries. The finite-fault slip distribution models are the shallowly dipping solution shown in Figure 8a and the steeply dipping solution in Figure 8b.

On the megathrust, the Coulomb stress increase ranges from about 4.8 bars in the positive thrusting direction (red color) to −3.5 bar decrease (blue color) for the shallowly dipping fault model. For the steeply dipping fault model, the Coulomb stress increase is up to 15.3 bars and the decrease is −13.4 bars, but these values are rather unstable because the main shock fault model terminates close to the megathrust. The zone of
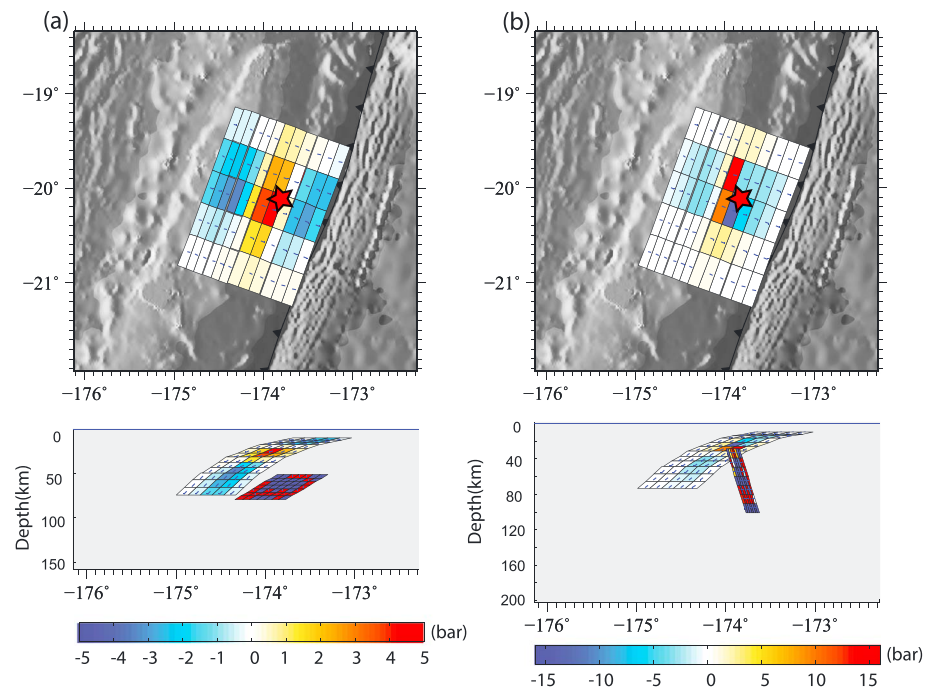
Figure 12. Coulomb stress changes that act in the direction of interplate thrust faulting on the megathrust calculated for faulting models for the 3 May 2006 event using (a) the shallowly dipping finite-fault solution in Figure 8a and (b) the steeply dipping finite-fault solution in Figure 8b. The map views show the stress changes on the target fault, with red stars representing the epicenter location; the vertical sections below are oblique views of the geometry of the intraslab fault relative to the megathrust fault.

increased driving stress is slightly downdip from the point above the hypocenter for the shallowly dipping intraslab faulting. This locates updip from the primary aftershock zone, which extends deeper on the megathrust (Figure 5). The steeply dipping intraslab faulting produces a downdip peak in driving stress at slightly greater depth, but the stress changes are localized and still do not extend down to where the aftershocks concentrate. Both rupture models induce reductions of driving stress on the shallow megathrust. Both rupture models also produce several bar increases on normal faulting orientations seaward of the hypocenter at 15 km depth where extensional faulting is observed (not shown), but driving stress is negative for normal faulting close to the toe of the upper plate wedge. To first order, these tendencies do not depend on details of the slip distribution or precise fault placement.

Earthquakes in the Tonga region have a high b value [*Frohlich and Davis*, 1993], which indicates that a large component of the seismic deformation involves smaller earthquakes. The 2009 Samoa normal faulting earthquake triggered widespread seismicity around northern Tonga in addition to the triggered coseismic megathrust failure [*Lay et al.*, 2010]. It is not clear whether the southern Tonga region responds similarly, with widespread activation by strong shaking or whether triggering of coseismic rupture is needed to account for the aftershocks. Evaluation of the regional behavior to future large regional faulting may help to resolve this issue.

3. The 19 March 2009 Sequence

On 19 March 2009, another large (m_b 7.0, M_S 7.6; USGS-NEIC) compressional faulting earthquake occurred below the Tonga trench about 300 km south of the 3 May 2006 earthquake (Figure 2). USGS-NEIC locates this event at 23.04°S, 174.66°W, 31.0 km deep, at 18:17:40 UTC. The GCMT centroid location is 23.08°S, 174.23°W, 49.1 km deep, with a seismic moment of 3.4×10^{20} Nm (M_w 7.6) and a centroid time shift of 12.3 s. The GCMT best double-couple solution (plane 1: strike = 205°, dip = 44°, slip = 98°; plane 2: strike = 14°, dip = 46°, slip = 82°) appears to have too high of a dip to involve thrusting on the shallowly dipping megathrust.
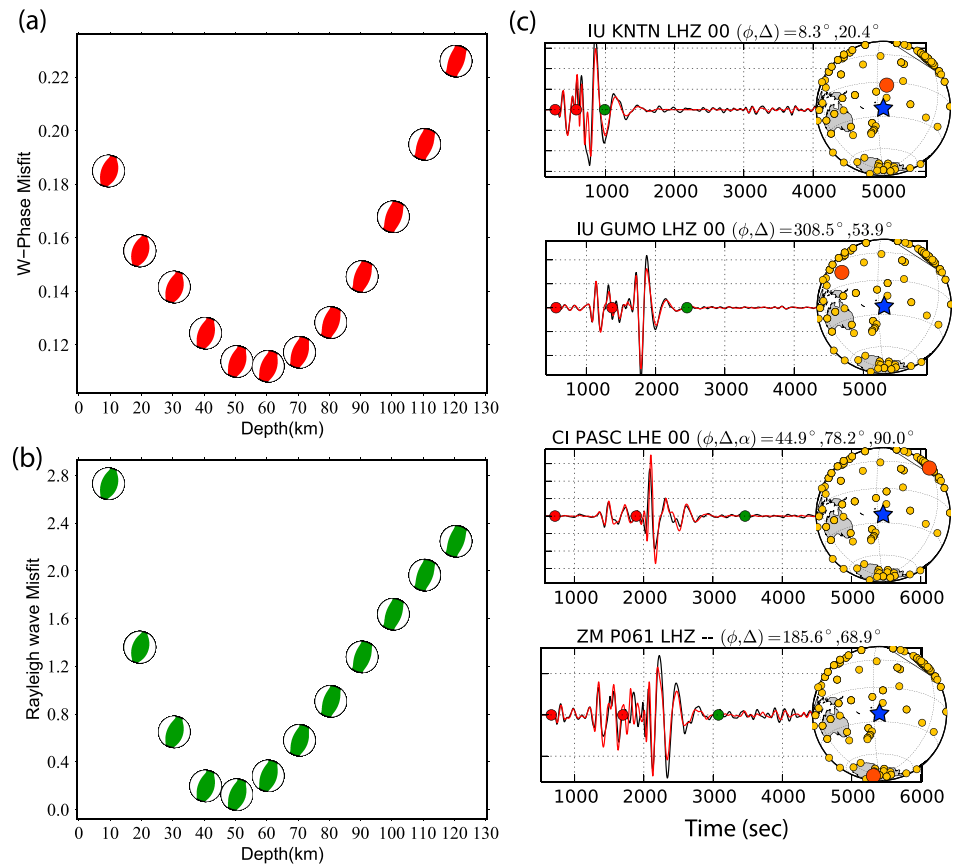
Figure 13. Residual waveform misfit for ground displacements in the 3.33 to 10 mHz passband versus point-source depth for (a) W-phase inversions (red focal mechanisms for each depth) and for (b) observed and predicted Rayleigh wave signals using the W-phase solution at each depth (green focal mechanisms) for the 19 March 2009 Tonga event. Example observed (red lines) and synthetic (black line) waveforms are shown on the right. The time window between the red dots is used for the W-phase inversions, and the time window between the second red dot and green dot is used for predicted Rayleigh wave misfit calculation. The gold dots on the maps are the positions of all stations used in the inversion with the red dot indicating the position of the specific station shown. The blue star indicates the source epicenter.

We performed W-phase inversions of 168 three-component ground motions in the 3.33 to 10 mHz passband, for source depths of 10 to 120 km, obtaining a residual misfit curve (shown by red focal mechanisms in Figure 13a) near a centroid depth of about 60 km. The misfit of predicted vertical component Rayleigh waves in the same passband for the W-phase inversion at each source depth has a residual misfit curve with a well-defined minimum (Figure 13b) near a depth of 50.5 km, similar to the GCMT centroid depth result. *Duputel et al.* [2012] obtained a centroid depth of 50.5 km with M_w 7.6, using somewhat different data and passband. These long-period solutions and the location of the hypocenter near the Tonga trench axis indicate rupture within the Pacific plate.

We do not have local GPS data for this earthquake due to its location, so we determine the finite-fault slip model using 93 broadband teleseismic *P* and *SH* wave ground motion recordings in the 1 to 200 s period range. The teleseismic locations of aftershocks again do not indicate a clear choice of fault plane (Figure S6a), so we consider both possible geometries. Figure 14 shows the source time function, average focal mechanism, and slip distribution of the finite-fault model using the eastward dipping fault with strike 14° and dip 46°. The fault model extends 60 km along dip and 70 km along strike with 10 km grid spacing. The subfault source time function parameterization and rupture expansion velocity are the same as for the 3 May 2006 event. The estimated moment is 3.5×10^{20} Nm, and the centroid time shift is 12.6 s. Figure S7 shows all of the observed *P* and *SH* waveforms (black) and synthetic seismograms (red) predicted by
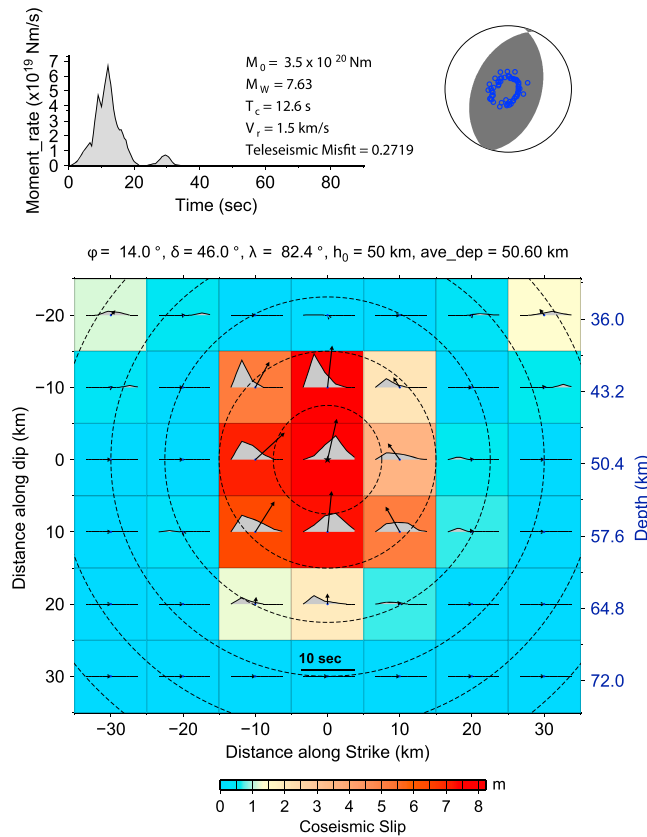
Figure 14. (bottom) Finite-fault slip distribution for the eastward dipping fault plane model of the 19 March 2009 Tonga event from inversion of teleseismic body waves (*P* and *SH*). Vectors in each subfault indicate the average subfault rake and slip magnitude, which is also color-coded. (top) The moment rate function and lower hemisphere focal mechanism with *P* wave sampling points are shown. Rupture expansion velocity is 1.5 km/s, with the rupture front indicated by dashed circles at 5 s intervals. The hypocenter is 50.4 km deep.

finite-fault model in Figure 14. The waveform fits are quite good for *P* waves, but some *SH* signals to the NW and NE are not well modeled. The location of the source below the trench may enhance azimuthal variations in the Green's functions that are not well accounted for by the local CRUST 1.0 velocity structure.

The solution for the westward dipping finite-fault model, with strike 205° and dip 44°, is not shown here but fits the observed teleseismic waveforms as well as the eastward dipping finite-fault model. Thus, we again cannot reliably establish which is the actual fault plane. The USGS-NEIC website presents a preliminary finite-fault solution (http://earthquake.usgs.gov/earthquakes/eventpage/usp000gv5p#scientific_finitefault) for a westward dipping plane with strike 205° and dip 50°, which they find to fit the data better, with a concentrated slip patch extending from 35 to 55 km depth, similar to our inversions.

4. Source Spectra and Radiated Energy

We determined the moment rate spectra of the 2006 and 2009 Tonga events, using the moment rate functions from finite-fault inversions for frequencies below 0.05 Hz and average spectra of teleseismic *P* waves corrected for geometric spreading, radiation pattern, and attenuation for frequencies from 0.05 to 1.0 Hz. These moment rate spectra are shown in Figure 15, along with reference spectra for ω-squared spectra with the same seismic moments and stress parameters of 3 MPa. The spectral levels for frequencies above 0.4 Hz tend to exceed those of the reference spectra, which is typical of intraplate ruptures [e.g., *Ye et al.*, 2013a]. We apply the method of *Venkataraman and Kanamori* [2004] and *Ye et al.* [2012] to calculate the radiate energy for each event using the *P* wave ground velocity recordings with corrections for low-frequency contributions based on the source spectra, finding radiated energy estimates of $E_R = 3.4 \times 10^{16}$ J for the 3 May 2006 event and $E_R = 8.3 \times 10^{15}$ J for the 19 March 2009 event.

The seismic moment-scaled radiated energy E_R/M_0, using the GCMT moment for each event, is 3.1×10^{-5} for the 3 May 2006 event and 2.2×10^{-5} for the 19 March 2009 event. These values are consistent with results for other large intraplate and intraslab events (Figure 15). We computed the stress drop, $\Delta\sigma$, for our main shock finite-fault models following the method of *Noda et al.* [2013] and then calculated the radiation efficiency, η_R, based on the equation $\eta_R = E_R/\Delta W_0 = (2\mu E_R/M_0)/\Delta\sigma$ [*Venkataraman and Kanamori*, 2004]. We find that the 2006 Tonga event has a stress drop of 22 MPa with radiation efficiency of 0.09, while the 2009 Tonga event has a stress drop of 25 MPa and radiation efficiency of 0.15. The low rupture velocity of 1.5 km/s used is compatible with the low seismic efficiency, high stress drop ruptures relative to single crack models in homogeneous media [e.g., *Ye et al.*, 2013b]. While the parameters are not uniquely resolved, it appears that rather dissipative processes were involved in both intraplate ruptures.
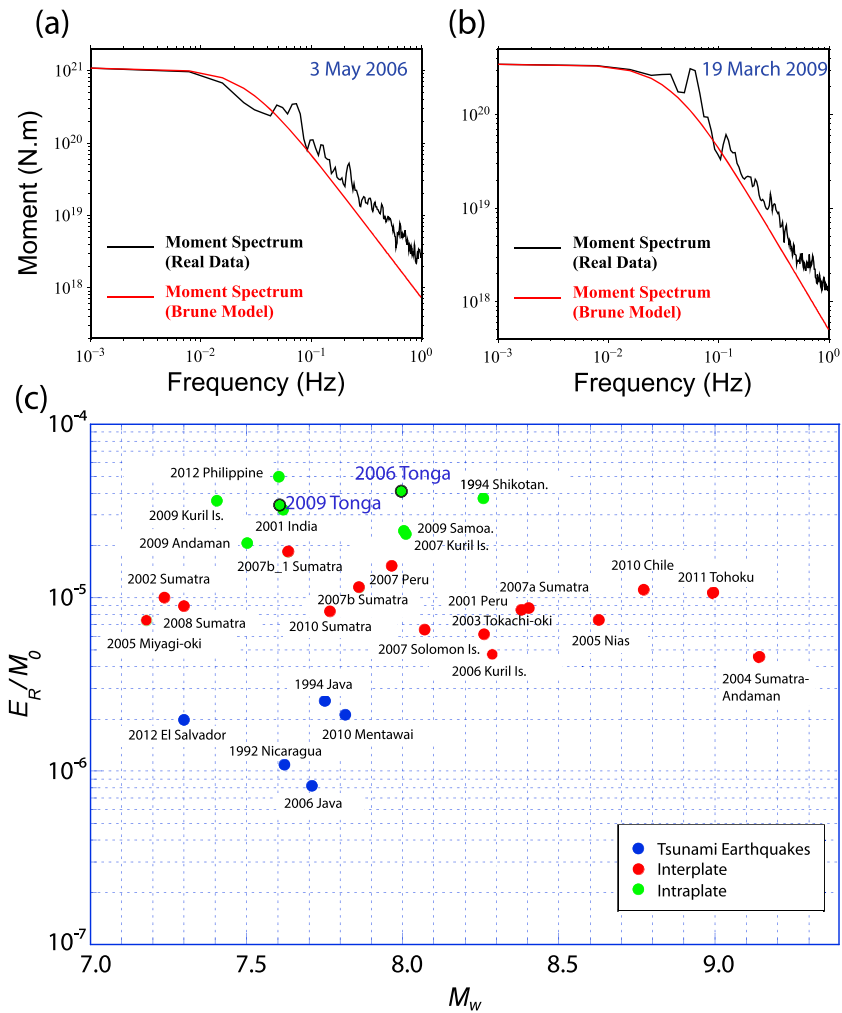
Figure 15. Source spectra of (a) the 3 May 2006 and (b) the 19 March 2009 Tonga events. The black lines are the spectra calculated using the source time function from finite-fault inversion for frequencies below 0.05 Hz and the average spectra of teleseismic body waves for frequencies from 0.05 Hz to 1.0 Hz. The red lines are reference spectra for an ω-squared model with 3 MPa stress parameter for the seismic moment for each event. (c) The moment-scaled radiated energy values for the two Tonga events along with corresponding determinations for other large intraslab events (green dots) and interplate events (red dots), with interplate tsunami events being shown in blue.

5. Discussion

Complex rupture in the northern Tonga subduction zone has previously been observed, most notably during the 29 September 2009 tsunamigenic earthquake sequence in Samoa [*Beavan et al.*, 2010; *Lay et al.*, 2010]. In contrast to the 2009 Samoa earthquake, however, for the 2006 Tonga earthquake the relative locations and mechanisms of the initial main shock and any triggered megathrust event are not distinct enough to detect by GPS coseismic deformation analysis [*Beavan et al.*, 2010] or backpropagation of teleseismic short-period signals [*Lay et al.*, 2010]. We applied backprojection of short-period *P* wave for several large networks of stations for the 2006 Tonga event without finding new constraints on the rupture. Differing results for W-phase versus GCMT focal mechanisms are an indicator of complex rupture [e.g., *Lay et al.*, 2010], but we find that these methods produce very similar results for the 2006 Tonga earthquake. This could be due to a small lateral separation in intraslab and megathrust ruptures and similarity of the focal mechanisms, if there was triggered coseismic slip. However, any slip on the megathrust would have to have small seismic moment, given the long-period centroid depths and lack of success in identifying any megathrust faulting in our multiple fault inversions.

Our interpretation of the 2006 event aftershock sequence is that most of the activity is on or near the megathrust, so significant faulting was induced by the intraplate event. Similarly, the larger aftershocks for the 2009 event have shallow focal mechanisms consistent with interplate faulting (Figure S6b), and it is likely that these are all megathrust failures as well. Triggering of slip on the megathrust in the Tonga subduction zone by intraplate ruptures could generally be more pronounced than in other regions due to the apparently weak seismic coupling, and this may account for the aftershock sequence for both the 2006 and 2009 events. However, we cannot make any statement from our analysis about megathrust coupling further to the north or south than the aftershock region. The sparse number of available GPS stations and their distance from the trench yield large uncertainties in estimates of slip deficit in the region of the 2006 earthquake. While we are convinced that the 2006 event was not on the plate boundary, our ability to translate that information into an assessment of the degree of seismic coupling of the regional megathrust is very limited. For example, large shallow intraslab normal faulting and compressional faulting in 2006 occurred in Northern Kermadec and triggered significant interplate thrust faulting [*Todd and Lay*, 2013]. However, the megathrust in that region has hosted the largest recorded interplate events in Kermadec and has clear evidence of slip-deficit accumulation from GPS observations over the past few decades, so one cannot make a general statement that the triggering of megathrust aftershocks implies low seismic coupling.

The large centroid depth of the 2006 Tonga event appears to account for the small tsunami that was observed. The Pacific Tsunami Warning Center had issued a regional tsunami warning for the islands of Tonga, Niue, American Samoa, Samo, Fiji, and New Zealand within 16 min of the earthquake, but it was canceled about 2 h later when the largest tsunami observed on ocean buoys was less than 60 cm. The limited deep water observations from Deep-ocean Assessment and Reporting of Tsunami stations near Hawaii were modeled by *Tang et al.* [2008], using the Method of Splitting Tsunami procedure, showing that a generic shallow-dipping thrust solution produces a good fit to the waveforms with a slip of 1 m. However, there is little sensitivity to precise mechanism or depth in the remote signals, and the larger slip and greater depth of our seismological models can account for the tsunami excitation in general. Lacking detailed bathymetry around the Tonga Islands, we have not attempted to model the moderate local tsunami in this study.

The analysis of the two large compressional faulting earthquakes in southern Tonga confirms that both involve intraslab faulting, below the megathrust. The largest known interplate seismogenic faulting on the Tonga megathrust remains the triggered faulting that occurred during the 29 September 2009 Samoa earthquake. This leaves the seismic hazard very uncertain and adds to the need for seafloor geodetic determinations of slip deficit along the arc to clarify the proportion of plate motion that is aseismic.

6. Conclusions

The 3 May 2006 (M_w 8.0) and 19 March 2009 (M_w 7.6) earthquakes are large compressional faulting intraslab events in southern Tonga. Analysis of long-period ground motions and broadband P and SH waves confirms that the rupture depths are located below the megathrust boundary in both events. Neither event has an unambiguously defined fault plane based on aftershocks or seismic wave observations. Finite-fault inversions for the candidate fault planes of the 2006 event using teleseismic and regional GPS static offset measurements do not uniquely resolve which is the rupture plane as long as a modest shift of the fault position is allowed. Aftershocks for the 2006 event suggest that some level of megathrust activation occurred, possibly involving coseismic triggered slip, but such a secondary rupture is not required in order to fit teleseismic body waves and local GPS static motion measurements. The fault plane for the 2009 event is also not well resolved, and aftershocks appear to again be near the megathrust. Regionally weak seismic coupling of the megathrust may account for efficient activation of interplate activity by the intraslab ruptures, by static and dynamic stresses. Southern Tonga continues to have a paucity of large megathrust earthquakes, leaving the seismic hazard in the region very uncertain and in need of direct assessment of fault zone slip-deficit accumulation using seafloor geodesy techniques.

References

Abercrombie, R. E., M. Antolik, and G. Ekström (2003), The June 2000 M_w 7.9 earthquakes south of Sumatra: Deformation in the India–Australia Plate, *J. Geophys. Res.*, *108*(B1), 2018, doi:10.1029/2001JB000674.

Altamimi, Z., X. Collilieux, J. Legrand, B. Garayt, and C. Boucher (2007), ITRF2005: A new release of the International Terrestrial Reference Frame based on time series of station positions and Earth orientation parameters, *J. Geophys. Res.*, *112*, B09401, doi:10.1029/2007JB004949.

Ammon, C. J., H. Kanamori, and T. Lay (2008), A great earthquake doublet and seismic stress transfer cycle in the central Kuril Islands, *Nature*, *451*, 561–565, doi:10.1038/nature06521.

Beavan, J., X. Wang, C. Holden, K. Wilson, W. Power, G. Prasetya, M. Bevis, and R. Kautoke (2010), Near-simultaneous great earthquakes at Tongan megathrust and outer rise in September 2009, *Nature*, *466*, 959–963, doi:10.1038/nature09292.

Berryman, K., et al. (2013), The GEM faulted Earth subduction characterization project, version 1.0, June 2013, *GEM Faulted Earth Project*. [Available at http://www.nexus.globalquakemodel.org/gem-faulted-earth/posts.]

Bevis, M., et al. (1995), Geodetic observations of very rapid convergence and back-arc extension at the Tonga arc, *Nature*, *374*, 249–251, doi:10.1038/374249a0.

Bird, P. (2003), An updated digital model of plate boundaries, *Geochem. Geophys. Geosyst.*, *4*(3), 1027, doi:10.1029/2001GC000252.

Bird, P., and Y. Y. Kagan (2004), Plate-tectonic analysis of shallow seismicity: Apparent boundary width, beta, corner magnitude, coupled lithosphere thickness, and coupling in seven tectonics settings, *Bull. Seismol. Soc. Am.*, *94*, 2380–2399.

Christensen, D. H., and L. J. Ruff (1988), Seismic coupling and outer rise earthquakes, *J. Geophys. Res.*, *93*(B11), 13,421–13,444, doi:10.1029/JB093iB11p13421.

Crawford, W. C., J. A. Hildebrand, L. M. Dorman, S. C. Webb, and D. A. Wiens (2003), Tonga Ridge and Lau Basin crustal structure from seismic refraction data, *J. Geophys. Res.*, *108*(B4), 2195, doi:10.1029/2001JB001435.

Dach, R., U. Hugentobler, P. Fridez, and M. Meindl (2007), Bernese GPS software version 5.0, Univ. of Bern.

DeMets, C., R. G. Gordon, and D. F. Argus (2010), Geologically current plate motions, *Geophys. J. Int.*, *181*, 1–80, doi:10.1111/j.1365-246X.2009.04491.x.

Dmowska, R., J. R. Rice, L. C. Lovison, and D. Josell (1988), Stress transfer and seismic phenomena in coupled subduction zones during the earthquake cycle, *J. Geophys. Res.*, *93*(B7), 7869–7884, doi:10.1029/JB093iB07p07869.

Duputel, Z., L. Rivera, H. Kanamori, and G. Hayes (2012), W phase source inversion for moderate to large earthquakes (1990–2010), *Geophys. J. Int.*, *189*, 1125–1147, doi:10.1111/j.1365-246X.2012.05419.x.

Dziewonski, A. M., and D. L. Anderson (1981), Preliminary reference Earth model, *Phys. Earth Planet. Int.*, *35*(4), 297–356, doi:10.1016/0031-9201(81)90046-7.

Frohlich, C., and S. D. Davis (1993), Teleseismic b values; or, much ado about 1.0, *J. Geophys. Res.*, *98*(B1), 631–644, doi:10.1029/92JB01891.

Gutenberg, B., and C. F. Richter (1954), *Seismicity of the Earth and Associated Phenomena*, 2nd ed., 310 pp., Princeton Univ. Press, Princeton, N. J.

Hartzell, S. H., and T. H. Heaton (1983), Inversion of strong ground motion and teleseismic waveform data for the fault rupture history of the 1979 Imperial Valley, California, earthquake, *Bull. Seismol. Soc. Am.*, *73*(6A), 1553–1583.

Hayes, G. P., D. J. Wald, and R. L. Johnson (2012), Slab1.0: A three-dimensional model of global subduction zone geometries, *J. Geophys. Res.*, *117*, B01302, doi:10.1029/2011JB008524.

Isacks, B., L. R. Sykes, and J. Oliver (1969), Focal mechanisms of deep and shallow earthquakes in the Tonga-Kermadec region and the tectonics of island arcs, *Geol. Soc. Am. Bull.*, *80*, 1443–1470.

Jordan, T. H., and K. A. Sverdrup (1981), Teleseismic location techniques and their application to earthquake clusters in the South-Central Pacific, *Bull. Seismol. Soc. Am.*, *71*(4), 1105–1130.

Kagan, Y. Y., and D. D. Jackson (2013), Tohoku earthquake: A surprise?, *Bull. Seismol. Soc. Am.*, *103*, 1181–1194, doi:10.1785/0120120110.

Kanamori, H., and L. Rivera (2008), Source inversion of W phase: Speeding up seismic tsunami warning, *Geophys. J. Int.*, *175*, 222–238, doi:10.1111/j.1365-246X.2008.03887.x.

Kennett, B. L. N., and E. Engdahl (1991), Traveltimes for global earthquake location and phase identification, *Geophys. J. Int.*, *105*, 429–465, doi:10.1111/j.1365-246X.1991.tb06724.x.

Kikuchi, M., and H. Kanamori (1991), Inversion of complex body waves—III, *Bull. Seismol. Soc. Am.*, *81*(6), 2335–2350.

Laske, G., G. Masters, Z. Ma, and M. Pasyanos (2013), Update on CRUST1.0—A 1-degree global model of Earth's crust, *Geophys. Res. Abstracts*, *15*, Abstract EGU2013-2658, 2013.

Lay, T., C. J. Ammon, H. Kanamori, L. Rivera, K. D. Koper, and A. R. Hutko (2010), The 2009 Samoa-Tonga great earthquake triggered doublet, *Nature*, *466*, 964–968, doi:10.1038/nature09214.

McCaffery, R. (1997), Statistical significance of the seismic coupling coefficient, *Bull. Seismol. Soc. Am.*, *87*, 1069–1073.

McCaffery, R. (2008), Global frequency of magnitude 9 earthquakes, *Geology*, *36*(3), 263–266.

Noda, H., N. Lapusta, and H. Kanamori (2013), Comparison of average stress drop measures for ruptures with heterogeneous stress change and implications for earthquake physics, *Geophys. J. Int.*, *193*, 1691–1712, doi:10.1093/gji/ggt074.

Okal, E. A. (1992), Use of the mantle magnitude Mm for the reassessment of the moment of historical earthquakes, I: Shallow events, PAGEOPH, 139, 17–57.

Okal, E. A., J. Borrero, and C. E. Synolakis (2004), The earthquake and tsunami of 1865 November 17: Evidence for far-field tsunami hazard from Tonga, *Geophys. J. Int.*, *157*, 164–174, doi:10.1111/j.1365-246X.2004.02177.x.

Okal, E. A., J. C. Borrero, and C. Chagué-Goff (2011), Tsunamigenic predecessors to the 2009 Samoa earthquake, *Earth Sci. Rev.*, *107*, 128–140.

Okamoto, T. (1994), Teleseismic synthetics obtained from 3-D calculations in 2-D media, *Geophys. J. Int* 118, doi:10.1111/j.1365-246X.1994.tb03988.x.

Pacheco, J. F., and L. R. Sykes (1992), Seismic moment catalog of large shallow earthquakes, 1900 to 1989, *Bull. Seismol. Soc. Am.*, *82*(3), 1306–1349.

Pacheco, J. F., L. R. Sykes, and C. H. Scholz (1993), Nature of seismic coupling along simple plate boundaries of the subduction type, *J. Geophys. Res.*, *98*(B8), 14,133–14,159, doi:10.1029/93JB00349.

Ruff, L. J., and H. Kanamori (1983), Seismic coupling and uncoupling at subduction zones, *Tectonophysics*, *99*, 99–117.

Scholz, C. H., and J. Campos (1995), On the mechanism of seismic decoupling and back-arc spreading in subduction zones, *J. Geophys. Res.*, *100*, 22,103–22,115, doi:10.1029/95JB01869.

Scholz, C. H., and J. Campos (2012), The seismic coupling of subduction zones revisited, *J. Geophys. Res.*, *117*, B05310, doi:10.1029/2011JB009003.

Storchak, D. A., D. Di Giacomo, I. Bondár, E. R. Engdahl, J. Harris, W. H. K. Lee, A. Villaseñor, and P. Bormann (2013), Public release of the ISC-GEM Global Instrumental Earthquake Catalogue (1900–2009), *Seismol. Res. Lett.*, *84*(5), 810–815, doi:10.1785/0220130034.

Tang, L., V. V. Titov, Y. Wei, H. O. Mofjeld, M. Spillane, D. Arcas, E. N. Bernard, C. Chamberlin, E. Gica, and J. Newman (2008), Tsunami forecast analysis for the May 2006 Tonga tsunami, *J. Geophys. Res.*, *113*, C12015, doi:10.1029/2008JC004922.

Toda, S., R. S. Stein, V. Sevilgen, and J. Lin (2011), Coulomb 3.3 graphic-rich deformation and stress-change software for earthquake, tectonic, and volcano research and teaching—User guide, *U.S. Geol. Surv. Open File Rep.*, *2011–1060*, p. 63. [Available at http://pubs.usgs.gov/of/2011/1060/.]

Todd, E. K., and T. Lay (2013), The 2011 Northern Kermadec earthquake doublet and subduction zone faulting interactions, *J. Geophys. Res. Solid Earth*, *118*, 1–13, doi:10.1029/2012JB009711.

Venkataraman, A., and H. Kanamori (2004), Observational constraints on the fracture energy of subduction zone earthquakes, *J. Geophys. Res.*, *109*, B05302, doi:10.1029/2003JB002549.

Wallace, L. M., R. McCaffrey, J. Beavan, and S. Ellis (2005), Rapid microplate rotations and backarc rifting at the transition between collision and subduction, *Geology*, *33*(11), 857–860, doi:10.1130/G21834.

Wang, R., F. L. Martín, and F. Roth (2003), Computation of deformation induced by earthquakes in a multi-layered elastic crust—FORTRAN programs EDGRN/EDCMP, *Comput. Geosci.*, *29*, 195–207, doi:10.1016/S0098-3004(02)00111-5.

Wiens, D. A. (1989), Bathymetric effects on body waveforms from shallow subduction earthquakes and application to seismic processes in the Kurile trench, *J. Geophys. Res.*, *94*, 2955–2972, doi:10.1029/JB094iB03p02955.

Ye, L., T. Lay, and H. Kanamori (2012), Intraplate and interplate faulting interactions during the August 31, 2012 Philippine Trench earthquake (M_w 7.6) sequence, *Geophys. Res. Lett.*, *39*, L24310, doi:10.1029/2012GL054164.

Ye, L., T. Lay, and H. Kanamori (2013a), Ground shaking and seismic source spectra for large earthquakes around the megathrust fault offshore of northeastern Honshu, Japan, *Bull. Seismol. Soc. Am.*, *103*(2B), 1221–1241, doi:10.1785/0120120115.

Ye, L., T. Lay, H. Kanamori, and K. D. Koper (2013b), Energy release of the 2013 M_w 8.3 Sea of Okhotsk earthquake and deep slab stress heterogeneity, *Science*, *341*, 1380–1384.

Yue, H., T. Lay, L. Rivera, C. An, C. Vigny, X. Tong, and J. C. Báez Soto (2014), Localized fault slip to the trench in the 2010 Maule, Chile M_w = 8.8 earthquake from joint inversion of high-rate GPS, teleseismic body waves, InSAR, campaign GPS, and tsunami observations, *J. Geophys. Res. Solid Earth*, *119*, 7786–7804, doi:10.1002/2014JB011340.

The 3 May 2006 (M_W 8.0) and 19 March 2009 (M_W 7.6) Tonga Earthquakes: Intraslab Compressional Faulting Below the Megathrust

Qingjun Meng,[1] David S. Heeszel,[2] Lingling Ye,[1] Thorne Lay,[1] Douglas A. Wiens[3], Minghai Jia[4], and Phil R. Cummins[5]

1Department of Earth and Planetary Sciences, University of California Santa Cruz, Santa Cruz, CA 95064, USA. (qimeng@ucsc.edu, tlay@ucsc.edu, lye2@ucsc.edu)

2U.S. Nuclear Regulatory Commission, Office of New Reactors, Washington, DC 20555-0001, USA (david.heeszel@gmail.com)

3Department of Earth and Planetary Sciences, Washington University, 1 Brookings Drive, Saint Louis, MO 63130, USA (doug@wustl.edu)

4Community Safety and Earth Monitoring Division, Geoscience Australia, Symonston ACT 2607, Australia (minghai.jia@ga.gov.au)

5Research School of Earth Sciences, The Australian National University, Acton ACT 0200, Australia (phil.cummins@anu.edu.au)

Corresponding author: T. Lay, (tlay@ucsc.edu)

Contents of this file

Figures S1 to S7

Introduction

This supporting information mainly provides more detailed information of teleseismic waveform fitting and GPS static offset fitting for 3 May 2006 and 19 March 2009 Tonga main-shocks and the aftershock distribution (of NEIC catalog) on two trench perpendicular profiles.
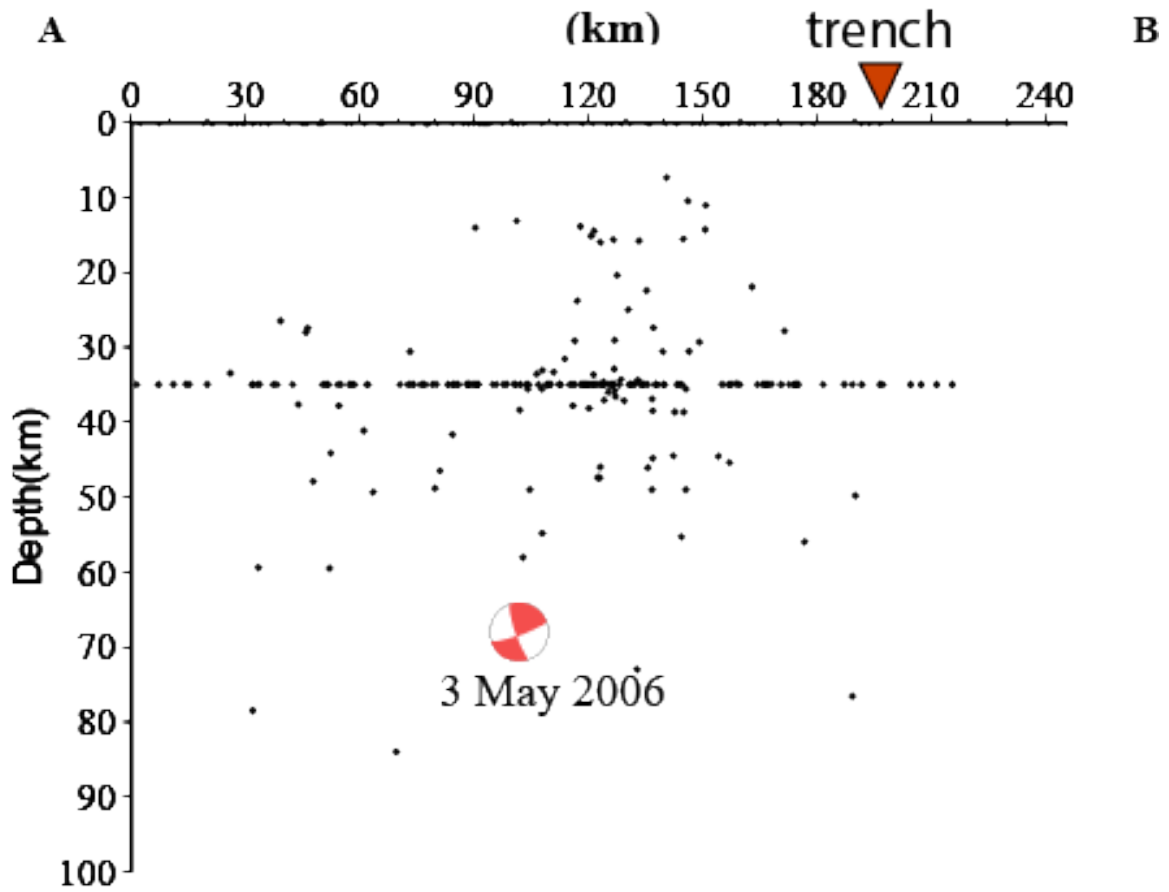
Figure S1. Cross-section view of aftershocks from the USGS-NEIC catalog for the 3 May 2006 Tonga event along profile AB in Figure 2. The scatter in the catalog locations is too large to confidently identify the megathrust, but the mainshock hypocenter clearly plots below the distributed aftershocks.
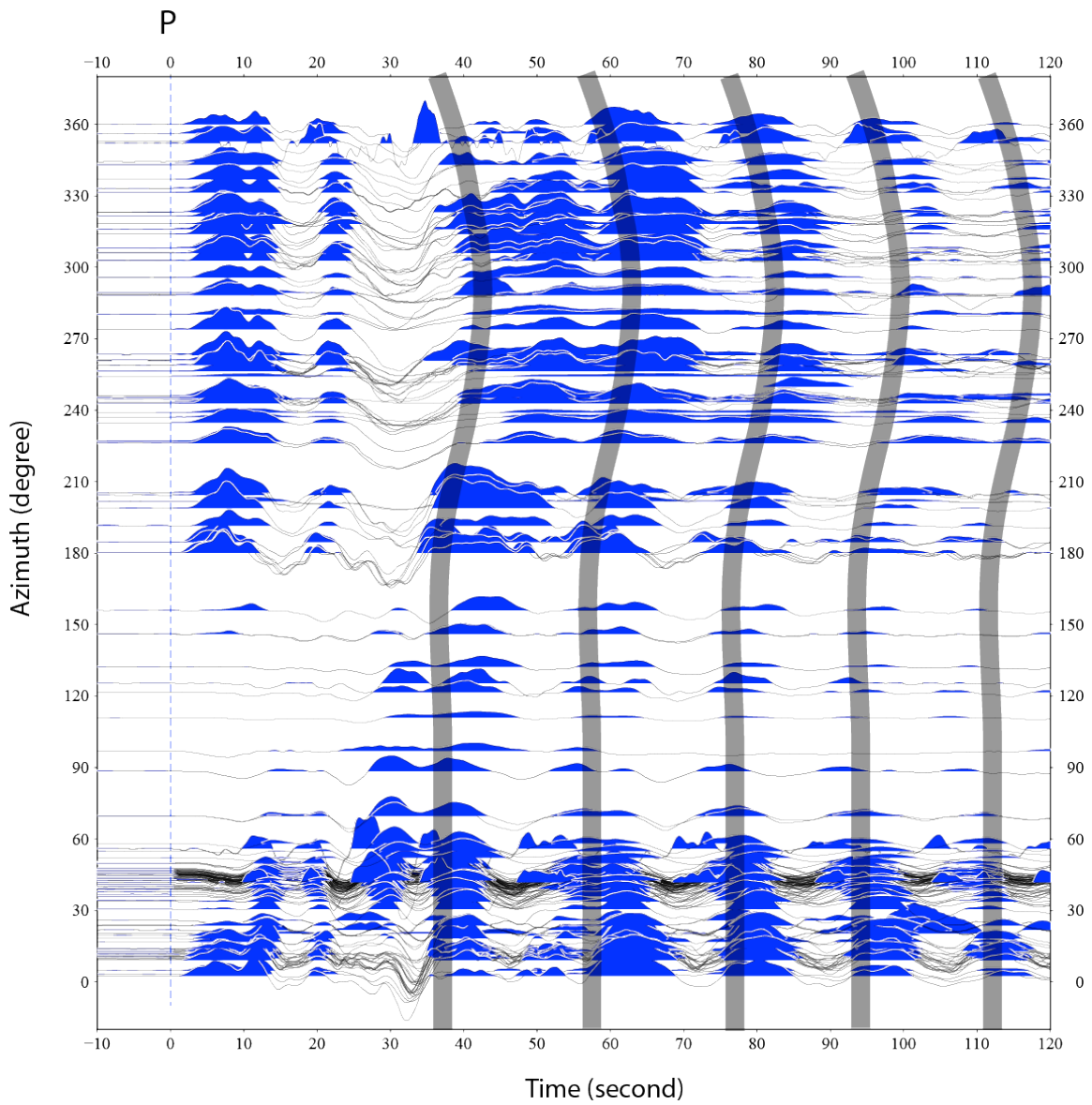
Figure S2. Azimuthal plot of the teleseismic P waveforms for the 3 May 2006 Tonga event, aligned on the P arrivals. Grey shadows indicate strong multiple water phase vibrations.
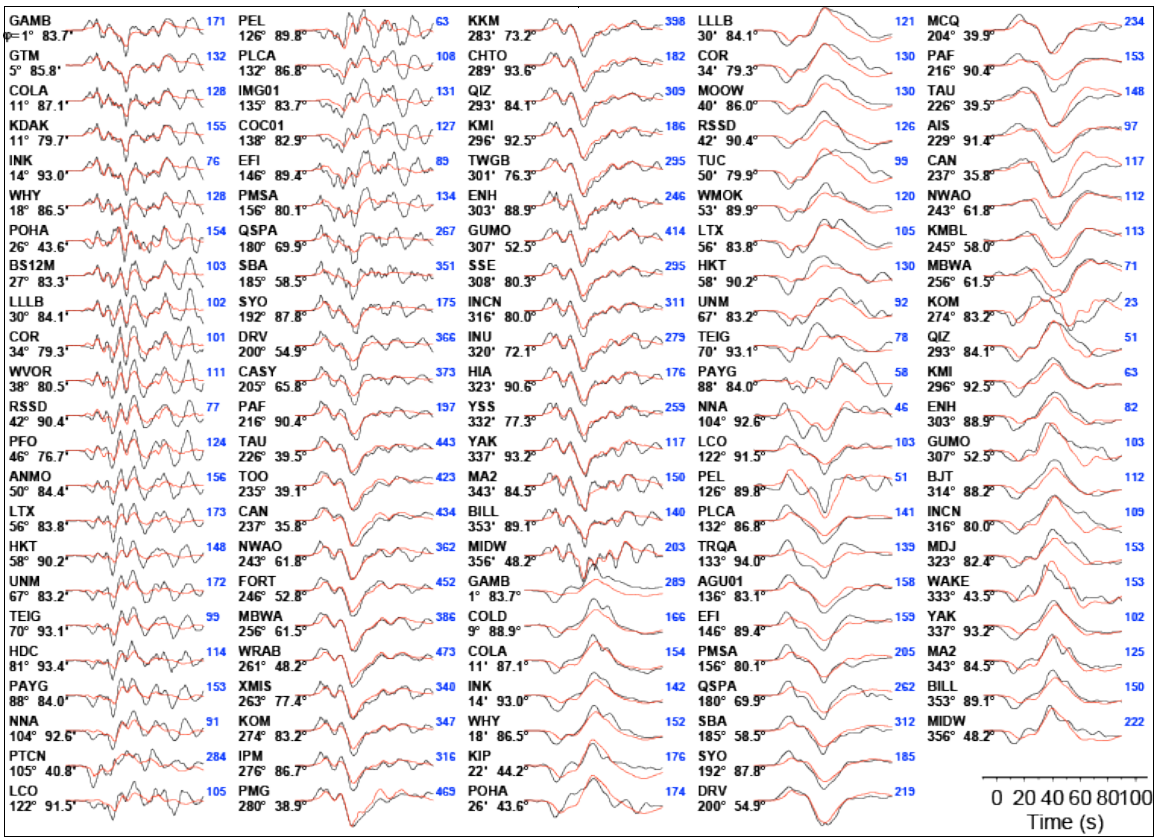
Figure S3. Observed (black) and predicted (red) teleseismic P and SH waveforms for the 3 May 2006 Tonga event for the joint inversion of teleseismic body waves and local static offsets for the shallowly dipping fault in Figure 8a.
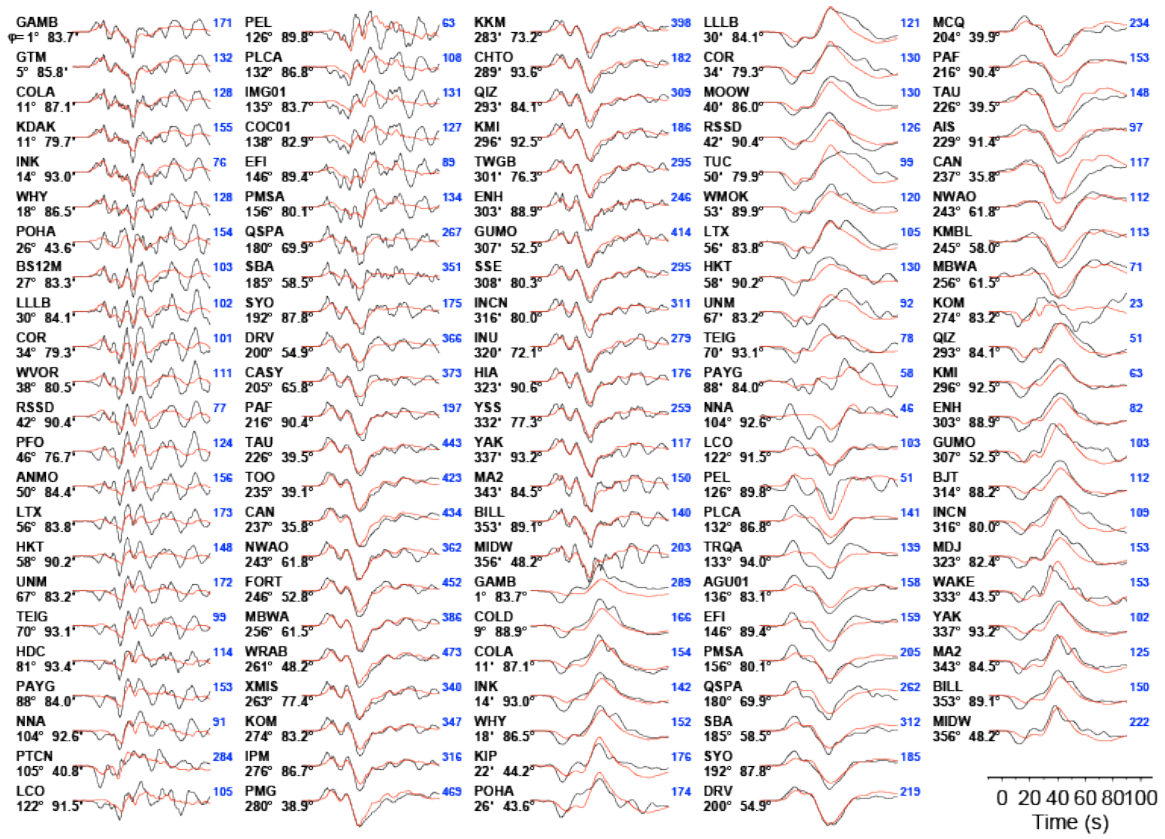
Figure S4. Observed (black) and predicted (red) teleseismic P and SH waveforms for the 3 May 2006 Tonga event for the joint inversion of teleseismic body waves and local static offsets for the steeply dipping fault in Figure 8b.
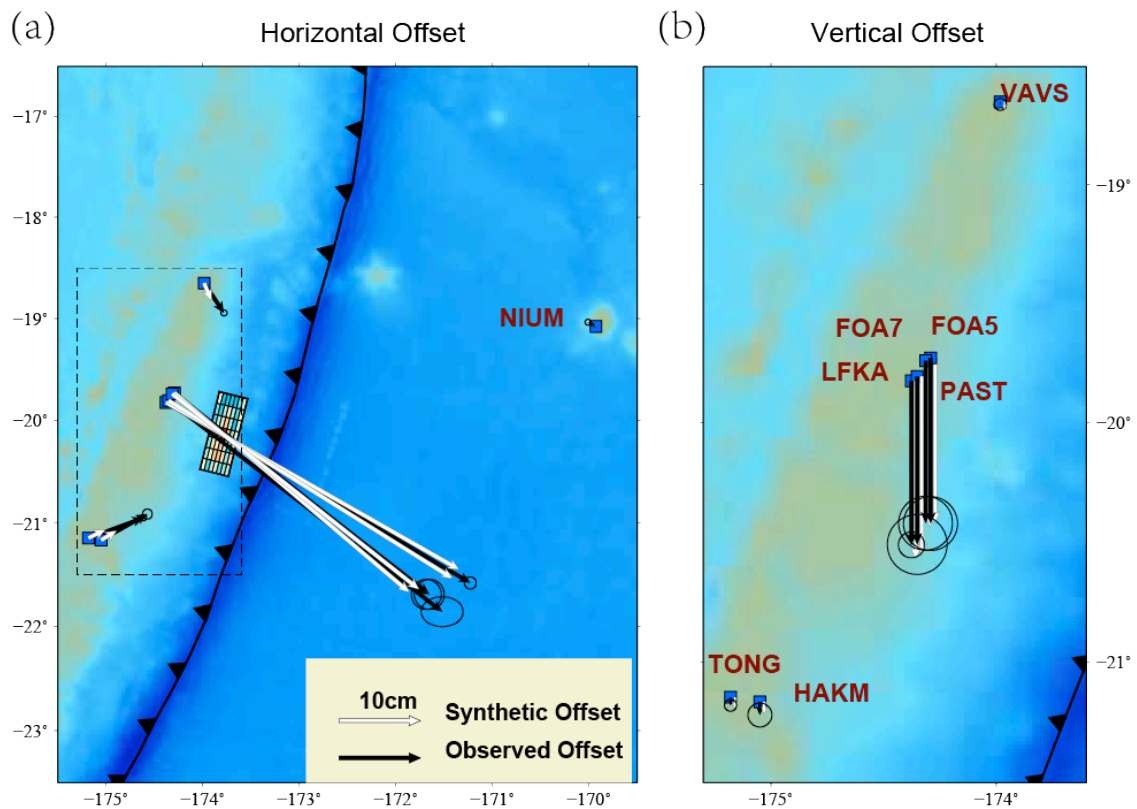
Figure S5. Locations of local GPS campaign stations (blue squares) that provide horizontal (black vectors in (a))and vertical (black vectors in (b))co-seismic offsets, within which (b) is a zoomed area of the dashed rectangle in (a), for the 3 May 2006 Tonga event. Their uncertainties (95% probability) are indicated by black ellipses. Predicted displacements for the steeply dipping fault plane model in Figure 8a are shown by red vectors for horizontal motions (a) and for vertical static offsets (b). The fits are comparable to those for the shallowly dipping fault plane shown in Figure 10.
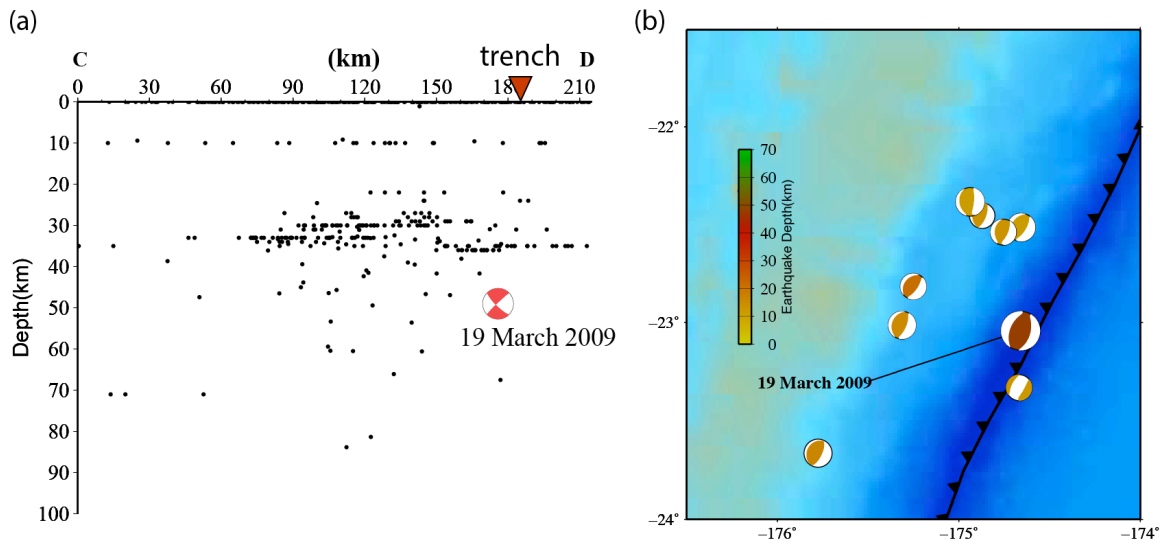
Figure S6. (a) Cross-section view of aftershocks from the USGS-NEIC catalog for the 19 March 2009 Tonga event along profile CD in Figure 2. The scatter in the unrelocated locations is too large to confidently identify the megathrust, but the mainshock hypocenter clearly plots below the distributed aftershocks and they are concentrated to the NW. (b) GCMT focal mechanisms of the mainshock and aftershocks in the following 3 months. The latter events range in magnitude from 5.0 to 5.5. All but one of the aftershocks has a shallow-dipping thrust fault mechanism. The thrust fault aftershocks have GCMT depths ranging from 12 to 22 km, and the normal faulting event below the trench has a depth of 13 km. It appears that megathrust faulting was induced by the deep intraplate compressional earthquake.
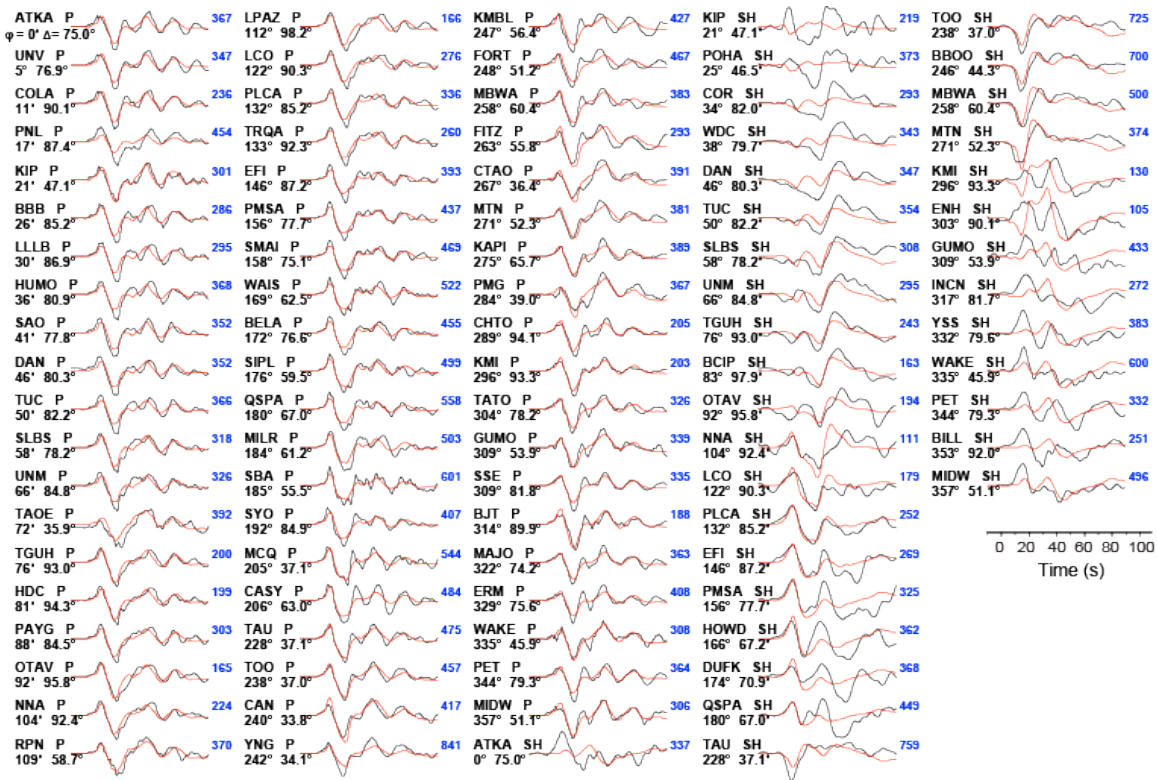
Figure S7. Observed (black) and predicted (red) teleseismic P and SH waveforms for the 19 March 2009 Tonga event for the inversion of teleseismic body waves for the eastward dipping fault shown in Figure 14.